Supplementary Information: Harnessing Automated SEM-EDS and Machine Learning to Unlock High-Throughput Compositional Characterization of Powder Materials

Andrea Giunto[1]*, Yuxing Fei[1,2], Pragnay Nevatia[3], Bernardus Rendy[1,2], Nathan Szymanski[1,2], Gerbrand Ceder[1,2]†

[1]Materials Sciences Division, Lawrence Berkeley National Laboratory, Berkeley, CA, USA
[2]Department of Materials Science and Engineering, University of California, Berkeley, CA, USA

[3]Department of Chemical and Biomolecular Engineering, University of California, Berkeley, CA, USA

Contents

*agiunto@lbl.gov
†gceder@berkeley.edu

1 Notes

1.1 Parameter calibration for peak shape modeling

Due to electronic noise in the detector, characteristic X-ray lines produce Gaussian peaks in energy-dispersive X-ray spectroscopy (EDS) spectra [1]:

$$G(E) = \frac{A}{\sigma\sqrt{2\pi}} \exp\left(-\frac{(E-\mu)^2}{2\sigma^2}\right) \tag{S1}$$

where E is the detector channel energy, A is the total peak area, μ is the characteristic line energy, and σ is the Gaussian standard deviation defining the peak full width at half maximum (FWHM, equal to 2.355σ). However, this ideal shape is systematically distorted by incomplete charge collection (ICC), which leads to peak asymmetry and low-energy tailing [2]. To account for these effects, various models have been proposed. By fitting high-count spectra (250k counts) from bulk, polished standards, we find that the skewed Gaussian model by Osán *et al.* [3]–excluding the low-energy shelf–best captures the observed peak shapes for line energies below 1.18 keV:

$$G_T(E) = G(E) + f_{\text{tail}} \times \frac{A}{2\gamma\sigma \exp\left(-\frac{1}{2\gamma^2}\right)} \exp\left(\frac{E-\mu}{\gamma\sigma}\right) \operatorname{erfc}\left(\frac{E-\mu}{\sqrt{2}\sigma} + \frac{1}{\sqrt{2}\gamma}\right) \tag{S2}$$

Here, γ is the skewness parameter, f_{tail} the tail fraction, and $\operatorname{erfc}(\cdot)$ is the complementary error function. For higher-energy lines above the silicon detector absorption edge at 1.84 keV, tailing diminishes and the peak shape generated by our EDS detector is better described by convolving a Gaussian with the ICC response function $f_{\text{icc}}(x)$ derived by Redus and Huber [2]:

$$G_{\text{Redus}}(E) = G(E) \circledast f_{\text{icc}}(E) \tag{S3}$$

where $\circledast$ denotes convolution; the function $f_{\text{icc}}(E)$ is defined via two parameters: the charge cloud radius R_e and the fraction of X-rays lost at the detector surface F_{loss} [2]. In the intermediate energy range (1.18–1.84 keV), we find that a hybrid model that convolves the skewed Gaussian with the ICC kernel best describes the peaks:

$$G_{T,\text{Redus}}(E) = G_T(E) \circledast f_{\text{icc}}(E) \tag{S4}$$

This composite approach enables accurate peak fitting and reliable peak deconvolution in multi-element compositions.

To obtain consistent peak modeling, we then calibrated the detector-specific shape parameters, namely γ, f_{tail}, R_e, F_{loss}, by fitting the peaks of ten 250k-count spectra of the bulk, polished EDS standards used throughout this work (see Methods:Quantification of EDS spectra). As shown in Supplementary Fig. 1, each parameter was modeled as a sigmoid function of line energy E, defined as:

$$f(E) = c + \frac{L}{1 + \exp[-k(E - x_0)]} \tag{S5}$$

where c is the baseline offset, L is the amplitude, x_0 is the sigmoid center (inflection point), k is the slope (steepness) of the transition. The best-fit coefficients for each peak-shape parameter are reported in Supplementary Tab. 1. These continuous, parametrized forms were subsequently held fixed during spectral fitting, ensuring a smooth and physically consistent description of detector ICC effects across the energy range probed in EDS.

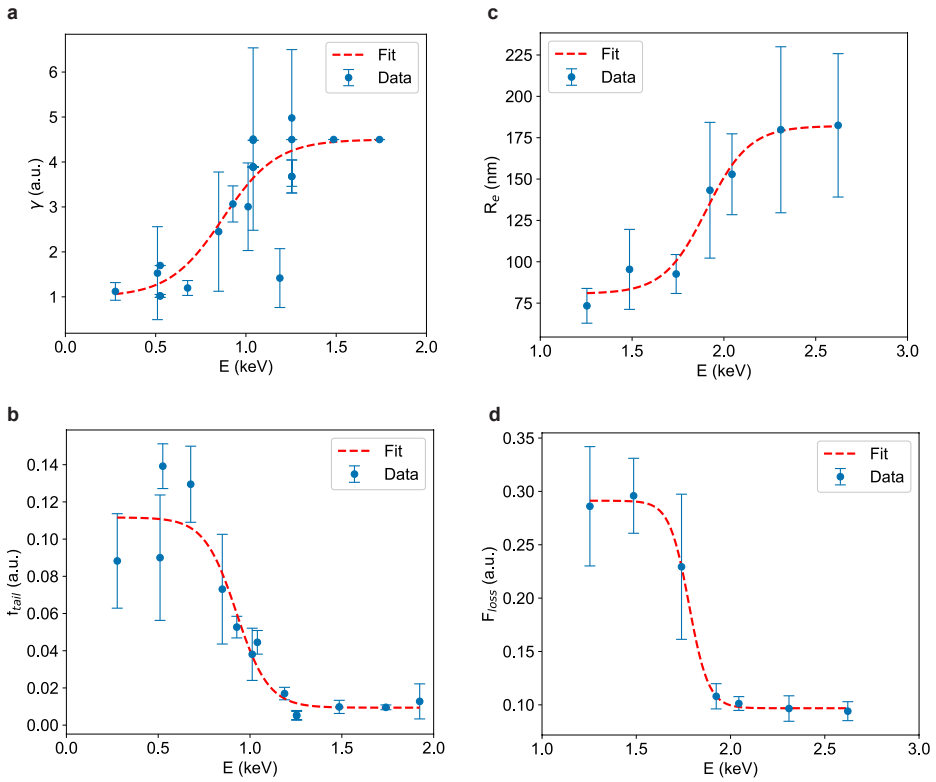

Supplementary Figure 1: **Parameter calibration for peak shape modeling accounting for ICC.** Peak parameters from Eqs. (S2) and (S3), fitted in function of characteristic line energy E of bulk, polished standards. **a**, Gaussian skewness parameter γ; **b**, Skewed Gaussian tail fraction f_{tail}; **c**, Radius of charge cloud forming in silicon drift detector (SDD) R_e; **d**, Fraction of X-rays lost at the detector surface F_{loss}. All parameters were fitted using a sigmoidal function (Eq. (S5)), with best-fits parameters reported in Supplementary Tab. 1.

Supplementary Table 1: **Fitted parameters for sigmoid functions modeling peak shape parameters as a function of characteristic line energy E.**

Parameter	c	L	x_0 (keV)	k
Skeweness parameter γ	1.00	3.50	0.88	9.63
Tail fraction f_{tail}	0.0094	0.1022	0.926	−11.42
Charge radius R_e (nm)	80.67	101.43	1.9051	8.60
Surface loss fraction F_{loss}	0.100	0.1912	1.7586	−40.3

1.2 Comparison of different atomic number averaging schemes

We evaluated the performance of different atomic number averaging schemes for compound materials, comparing three approaches: the method by Statham *et al.* [4], the formula proposed by Markowicz *et al.* [5], and the mass-fraction-based averaging employed by Lábár and Török [6]. Supplementary Fig. 2 shows $PB_{i,\mathbf{pure}}$ values obtained for K_α lines of O, Al, Si, and P from minerals and commercial precursors (see method described in Extended Data Fig. 5). In the three columns, the values of $PB_{i,\mathbf{pure}}$ were extracted from compounds using the background expression B_{gen} from this work–i.e. Eq. (13)–employing the three analyzed formulations of $\bar{Z}$. Across all four characteristic lines shown, the root-mean-squared relative error (RMSRE) of $PB_{i,\mathbf{pure}}$ values is lowest when using $\bar{Z}_{\text{Statham}}$, intermediate for $\bar{Z}_{\text{Markowicz}}$, and highest for the mass-weighted $\bar{Z}_w$. This indicates that $\bar{Z}_{\text{Statham}}$ provides a more accurate representation

of effective atomic number in compound materials for the purposes of background modeling, as argued in Ref. [4]. Plots for additional characteristic lines showing analogous trends are available online (see Code and data availability).

1.3 Calibration of P, F and β background model parameters

Parameters from the modified expression of Duncumb's generated background model–shape factor $P(Z)$, intensity scaling factor $F(Z)$, and attenuation factor $\beta(Z)$–were calibrated using 250k-count spectra from elemental bulk, polished standards acquired at 15 keV. For each standard, fitted parameters were averaged over approximately 15 spectra, and the resulting means with standard deviations are shown in Supplementary Fig. 3. Error-weighted least-squares fitting was performed for parametrization, using inverse squared data uncertainties as weights.

The pure-element spectra were initially fitted with $P(Z)$, $F(Z)$, and $\beta(Z)$ allowed to vary freely. Using the extracted parameters, an expression for $P(Z)$ was first determined, as this factor governs the spectral curvature of the generated continuum (see Extended Data Fig. 2b). As shown in Supplementary Fig. 3a, $P(Z)$ was best described by a second-order polynomial:

$$P(Z) = 0.00002041 \cdot Z^2 - 0.004076 \cdot Z + 1.252 \tag{S6}$$

With $P(Z)$ fixed, the spectral fitting process was repeated, and the newly found $\beta(Z)$ values were fitted using a composite empirical function combining a sigmoid and a Gaussian term, as shown in Supplementary Fig. 3b:

$$\beta(Z) = 0.0419 + \frac{0.2105}{1 + \exp\left(-0.4788 \cdot (Z - 45.9098)\right)} + 0.2807 \exp\left(\frac{-(Z - 28.0063)^2}{2 \cdot 4.6587^2}\right) \tag{S7}$$

We attribute the non-monotonic trend of $\beta(Z)$ to the presence/absence and position of low-energy characteristic X-ray lines across the different elements. Finally, spectral fitting was repeated with both $P(Z)$ and $\beta(Z)$ fixed, and the extracted values of intensity factor F were fitted using a sigmoid function, shown in Supplementary Fig. 3c:

$$F(Z) = 1 - \exp\left(-\frac{Z + 0.7453}{6.1543}\right) \tag{S8}$$

While we did not explicitly evaluate the dependence of these parameters on beam energy E_0, β is expected to vary as E_0 changes, reflecting the corresponding shift in the ratio of low- to high-energy bremsstrahlung. Duncumb *et al.* [7] describe P as Z-dependent and F as Z- and E_0-dependent, although not providing closed-form expressions for these parameters. On the other hand, Karamanov *et al.* [8] report full expressions of $P(Z, E_0)$ and $F(Z, E_0)$, finding that P is also dependent on E_0. These parametrized forms of P and F could not be applied here, as they are based on the unmodified Duncumb's background model without the attenuation factor β.

For compound materials, $F(Z)$ and $P(Z)$ are evaluated at the Statham average atomic number $\bar{Z}_{\text{Statham}}$ [4], following Eq. (8). In contrast, the strongly element-dependent shape of $\beta(Z)$ suggests that its evaluation at the compound average atomic number would be inappropriate. Instead, a mass-weighted average over elemental $\beta(Z_i)$ values is used:

$$\beta_{\mathbf{compound}} = \sum_i w_i \cdot \beta(Z_i) \tag{S9}$$

This averaging strategy is critical because β is incorporated into the generated background model (Eq. (9)) and directly affects the Z_c correction factor used to quantify elemental mass

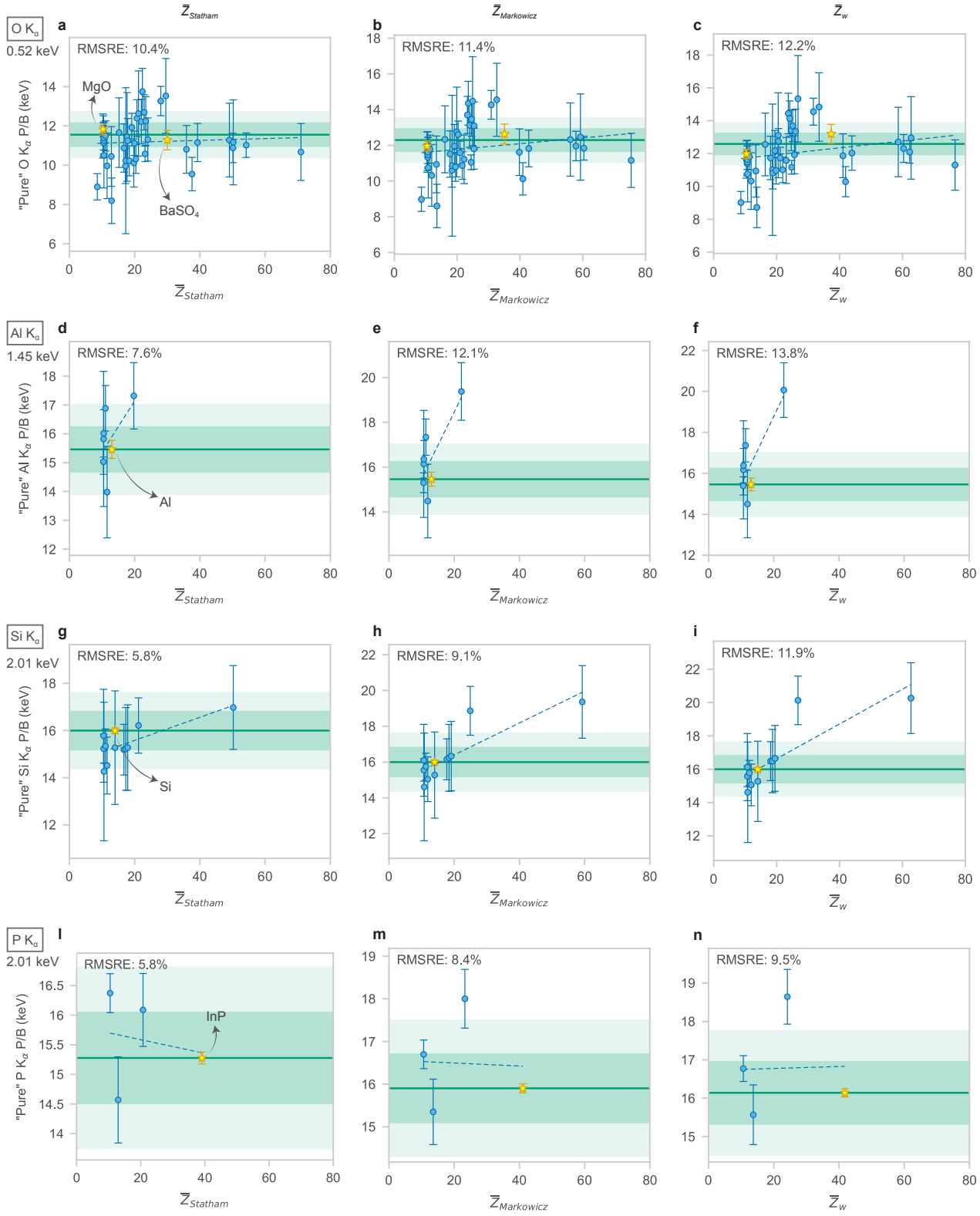

Supplementary Figure 2: **Performance of different atomic number averaging schemes for the purpose of background modeling.** Plots of $PB_{i,\mathbf{pure}}$ values extracted from minerals and commercial precursors (method described in Extended Data Fig. 5) using $\bar{Z}$ computed using the formulas proposed by (**first column**) Statham *et al.* [4], (**second column**) Markowicz *et al.* [5], and (**third column**) Lábár and Török [6]. Each row corresponds to a different K_α line, namely that of O, Al, Si, P, respectively from top to bottom.

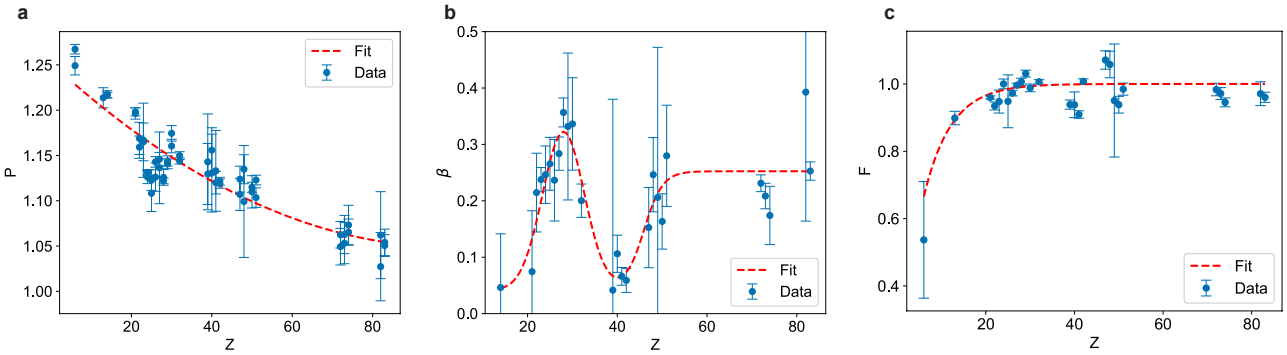

Supplementary Figure 3: **Calibration of background model parameters.** Fits of the shape (P), attenuation (β), and intensity scaling (F) factors in the generated background expression (Eqs. (7) and (9)), using polished elemental standards. **a**, Shape factor P; **b**, Attenuation factor β; **c**, Intensity factor F.

fractions w_i (Eq. (12)). To assess the effectiveness of this averaging approach, Supplementary Fig. 4 compares the values of $PB_{i,\mathbf{pure}}$ for selected K_α lines (N, O, Al), computed using either mass-averaged $\beta_{\mathbf{compound}}$ (top row) or $\beta(\bar{Z}_{\text{Statham}})$ (bottom row). A clear reduction in RMSRE is seen for low-energy lines (e.g., N, O K_α) when using mass-averaged β, whereas for higher-energy lines (e.g., Al K_α and others not shown), the effect is minimal or slightly adverse. This is consistent with the stronger influence of the attenuation factor β in the lower-energy portion of the EDS spectrum, as the background attenuation term $E/(E+\beta)$ approaches unity for large E. Overall, the significant accuracy gains at low energies validate the use of a mass-weighted β averaging scheme for compound materials.

1.4 Derivation of equations for EDS quantification with the P/B method

Elemental compositions are quantified from EDS spectra by relating the measured X-ray peak intensities to those obtained from standards of known composition. In a bulk, polished sample, the mass fraction of element i, denoted w_i, is quantified as:

$$w_i = \frac{I_i \cdot M_{c,I}}{I_{i,\text{std}} \cdot M_{c,I,\text{std}}} \cdot w_{i,\text{std}} \tag{S10}$$

where I_i and $I_{i,\text{std}}$ are the peak intensities for element i in the sample and standard, respectively; $w_{i,\text{std}}$ is the known elemental mass fraction in the standard; and $M_{c,I}$ is a factor correcting the peak intensity to remove matrix composition effects on electron backscattering, stopping power, X-ray absorption, and fluorescence [9].

By substituting the P/B-corrected intensity I^* from Eq. (2) (main text) in Eq. (S10), and expressing peak intensities as P instead of I, we obtain:

$$w_i = \frac{P_{i,p}}{B_{i,p}} \cdot \frac{B_{i,b}}{P_{i,\text{std}}} \cdot \frac{M_{c,P}}{M_{c,P,\text{std}}} \cdot w_{i,\text{std}} \tag{S11}$$

To include the experimental P/B values measured from bulk standards, we express $B_{i,b}/P_{i,\text{std}}$ as:

$$\frac{B_{i,b}}{P_{i,\text{std}}} = \frac{B_{i,\text{std}}}{P_{i,\text{std}}} \cdot \frac{B_{i,b}}{B_{i,\text{std}}} \tag{S12}$$

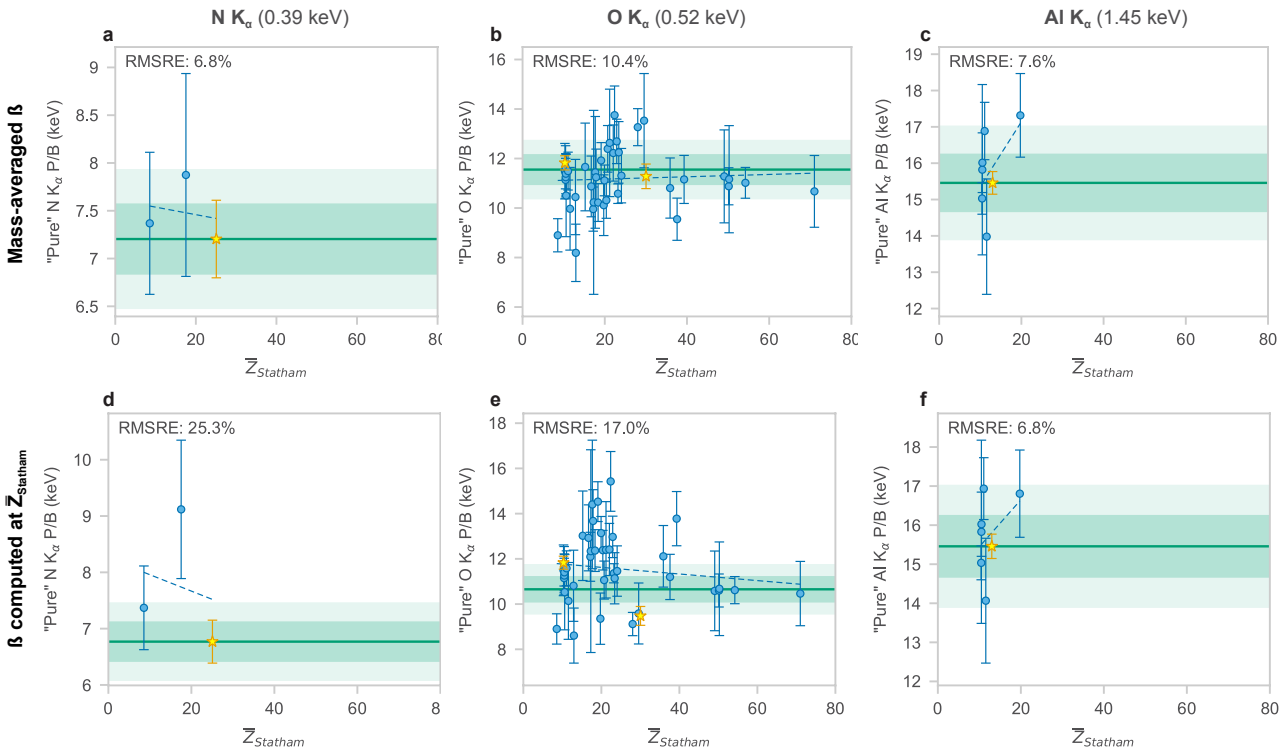

Supplementary Figure 4: **Effect of β averaging schemes for compound materials.** Values of $PB_{i,\mathbf{pure}}$ extracted from minerals and commercial precursors (see Extended Data Fig. 5), using two different averaging strategies for the attenuation factor β: **a**–**c**, mass-weighted averaging across the constituent elements; **d**–**f**, direct evaluation at the average atomic number $\bar{Z}$ computed using the method of Statham *et al.* [4], reported in Eq. (8).

Combining Eqs. (S11) and (S12), and including background matrix correction factors $M_{c,B}$ we obtain:

$$w_i = \frac{P_{i,p}}{B_{i,p}} \cdot \frac{B_{i,\mathrm{std}}}{P_{i,\mathrm{std}}} \cdot \frac{B_{i,b}}{B_{i,\mathrm{std}}} \cdot \frac{M_{c,P}}{M_{c,P,\mathrm{std}}} \cdot \frac{M_{c,B}}{M_{c,B}} \cdot \frac{M_{c,B,\mathrm{std}}}{M_{c,B,\mathrm{std}}} \cdot w_{i,\mathrm{std}} \tag{S13}$$

which can be rearranged to:

$$w_i = \underbrace{\frac{P_{i,p}}{B_{i,p}} \cdot \frac{M_{c,P}}{M_{c,B}}}_{\text{particle}} \cdot \underbrace{\frac{B_{i,\mathrm{std}}}{P_{i,\mathrm{std}}} \cdot \frac{M_{c,B,\mathrm{std}}}{M_{c,P,\mathrm{std}}} \cdot w_{i,\mathrm{std}}}_{\text{standard}} \cdot \underbrace{\frac{B_{i,b}}{B_{i,\mathrm{std}}} \cdot \frac{M_{c,B}}{M_{c,B,\mathrm{std}}}}_{Z_c} \tag{S14}$$

Here, $M_{c,P}$ and $M_{c,B}$ depend on composition and X-ray generation depth. Since they refer to the same sample, composition effects cancel out, and the similar generation depths for characteristic and continuum X-rays make $M_{c,P}/M_{c,B}$ close to unity. Remaining differences are captured as a second-order correction [6]:

$$\frac{M_{c,P}}{M_{c,B}} = R_c A_c F_c \tag{S15}$$

Substituting into Eq.(S14), we recover the formulation of Lábár and Török[6]:

$$w_i = \frac{P_{i,p}}{B_{i,p}} \cdot (P/B)^{-1}_{\mathrm{std}} \cdot R_c A_c F_c \cdot Z_c \tag{S16}$$

where $(P/B)_{\mathrm{std}}$ is the reference standard P/B value computed as $\frac{P_{i,\mathrm{std}}}{B_{i,\mathrm{std}}}(R_c A_c F_c)_{\mathrm{std}}/w_{i,\mathrm{std}}$. To compute Z_c, we observe that the term $B_{i,b} \cdot M_{c,B}$ quantifies the background intensity stripped

of matrix composition effects (B_{gen}). Hence:

$$Z_c = \frac{B_{i,b}}{B_{i,\mathrm{std}}} \cdot \frac{M_{c,B}}{M_{c,B,\mathrm{std}}} = \frac{B_{gen}(\bar{Z}_p)}{B_{gen}(\bar{Z}_{std})} \tag{S17}$$

1.5 Comparison of different Z_c correction schemes

We evaluate the performance of four different formulations of the correction term Z_c, which is used in the P/B quantification formula in Eq. (11). Supplementary Fig. 5 compares $PB_{i,\mathbf{pure}}$ values for representative characteristic lines (K_α for O, Na, Al, Si, P, Mn, Fe, Cu; L_α for Y; M_α for Pb), extracted from minerals and commercial precursors listed in Tab. 1 using four different Z_c correction schemes. Results for additional lines are available online (see Code and data availability). The first three columns replicate the correction methods shown in Extended Data Fig. 5. This work's approach (first column), which incorporates stopping power correction S and Statham's atomic number averaging [4], consistently yields the lowest RMSRE. Omitting the stopping power term (second column) significantly increases the RMSRE for all reported lines. The prior formulation of Z_c by Lábár and Török [6, 10] (third column) yields the highest RMSRE, reflecting its inability to account for composition-dependent variations in generated continuum intensity between sample and standard. The fourth column evaluates the empirical generated background model from Castellano *et al.* [11], implemented with stopping power correction. This correction consistently underperforms relative to *AutoEMXSp*'s correction scheme, suggesting that the modified Duncumb-based formulation proposed here offers a more accurate representation of the generated continuum.

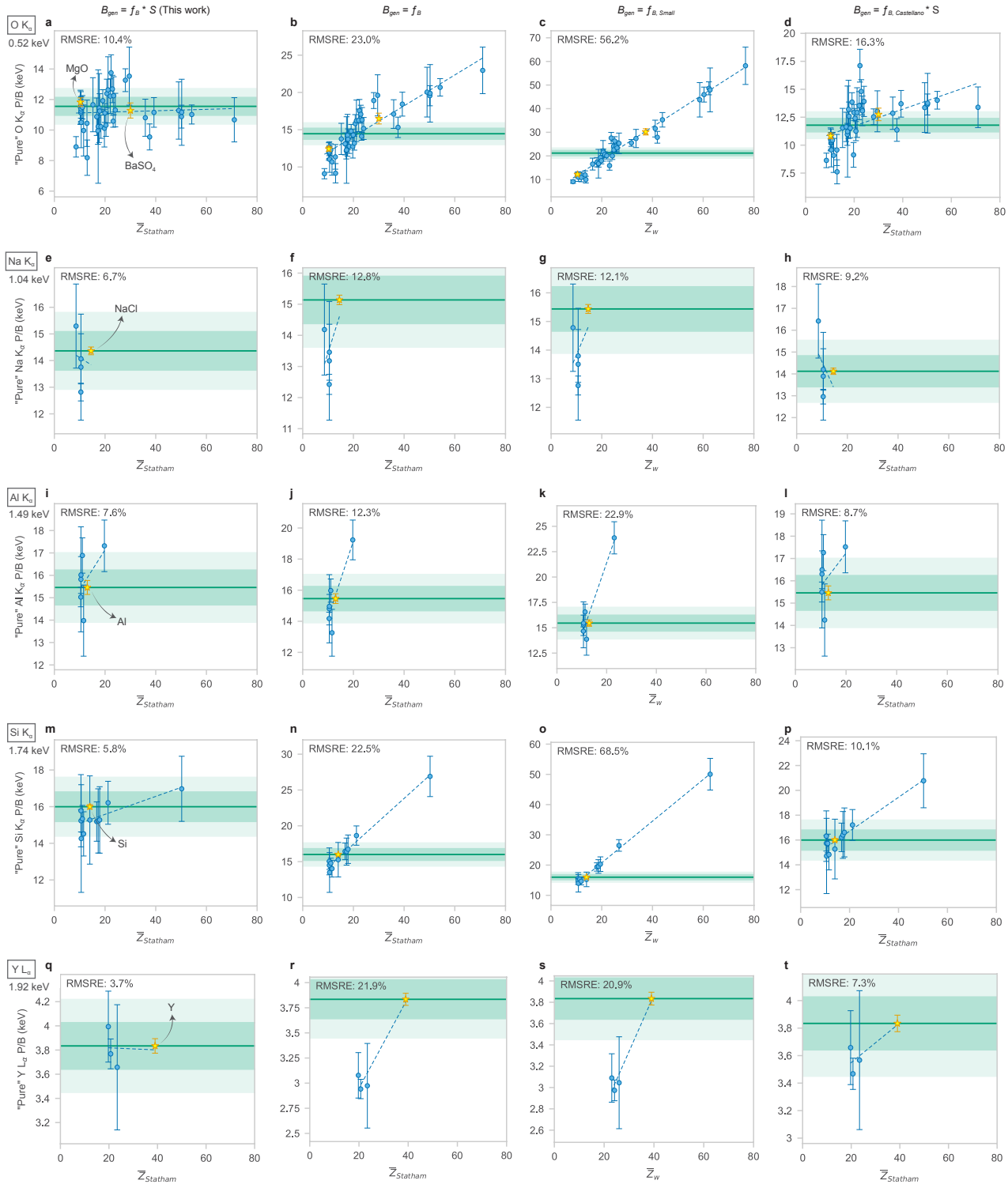
$B_{gen} = f_B * S$ (This work)
$B_{gen} = f_B$
$B_{gen} = f_{B,Small}$
$B_{gen} = f_{B,Castellano} * S$
O K_α
0.52 keV
Na K_α
1.04 keV
Al K_α
1.49 keV
Si K_α
1.74 keV
Y L_α
1.92 keV
RMSRE: 10.4%
RMSRE: 23.0%
RMSRE: 56.2%
RMSRE: 16.3%
RMSRE: 6.7%
RMSRE: 12.8%
RMSRE: 12.1%
RMSRE: 9.2%
RMSRE: 7.6%
RMSRE: 12.3%
RMSRE: 22.9%
RMSRE: 8.7%
RMSRE: 5.8%
RMSRE: 22.5%
RMSRE: 68.5%
RMSRE: 10.1%
RMSRE: 3.7%
RMSRE: 21.9%
RMSRE: 20.9%
RMSRE: 7.3%
MgO
$BaSO_4$
NaCl
Al
Si
Y
"Pure" O K_α P/B (keV)
"Pure" Na K_α P/B (keV)
"Pure" Al K_α P/B (keV)
"Pure" Si K_α P/B (keV)
"Pure" Y L_α P/B (keV)
$\overline{Z}_{Statham}$
$\overline{Z}_w$

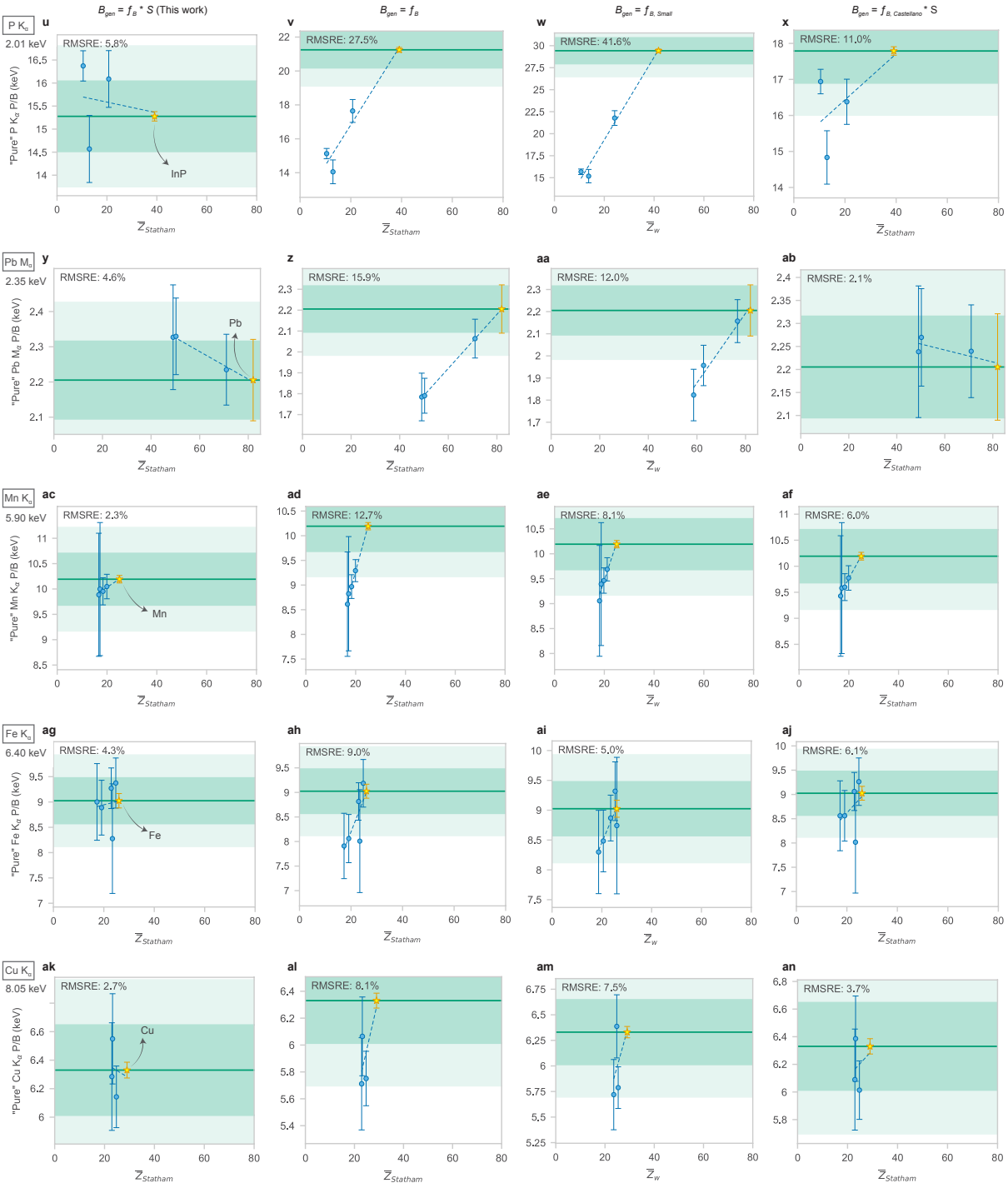

Supplementary Figure 5: **Comparison of different Z_c correction schemes.** Plots of $PB_{i,\mathbf{pure}}$ for a representative set of lines that include K_α for O, Na, Al, Si, P, Mn, Fe, Cu, L_α for Y and M_α for Pb, sorted vertically by increasing energy. Values of $PB_{i,\mathbf{pure}}$ are extracted from minerals and commercial powders listed in Tab. 1, following the procedure described in Extended Data Fig. 5. Columns show three different implementations of Z_c: **I column**, using *AutoEMXSp*'s generated background model B_{gen} with stopping power correction S and Statham's atomic number averaging ($\bar{Z}_{Statham}$, Eq. (8) [4]); **II column**, omitting S from the generated background term; **III column**, following prior formulation of Z_c from Lábár and Török [6, 10], where B_{gen} is set equal to the background model from Small *et al.* [12] and $\bar{Z}$ is mass-weighted ($\bar{Z}_w$). **IV column**, using Castellano *et al.* [11] generated background model, implemented with stopping power correction.

2 Additional sample characterization

2.1 SEM-EDS compositional map of $NaAlSiO_4$ + $LiMn_{1.5}Ni_{0.5}O_4$ mixture

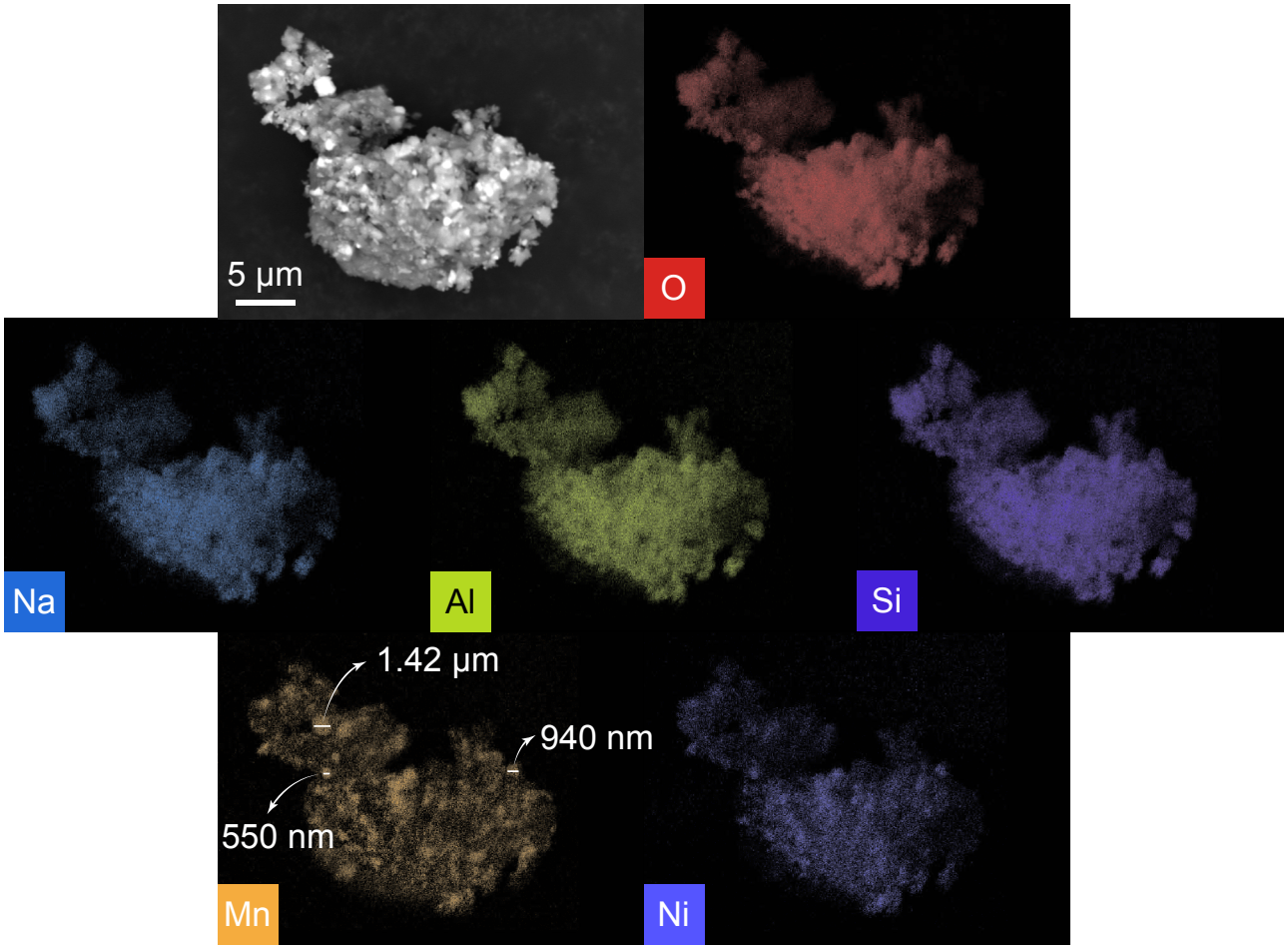

Supplementary Figure 6: **SEM-EDS characterization of the sample from Wang *et al.* [13], showing sub-micron to micron-scale intermixing of $NaAlSiO_4$ and $LiMn_{1.5}Ni_{0.5}O_4$.** SEM-EDS compositional mapping on a representative particle of approximately 15 µm × 25 µm, using K_α characteristic lines for all elements except Ni, for which the L_α line was employed. The compositional map reveals a homogeneous mixture of the two phases, showing numerous Mn–Ni–O particles (a few hundred nm to a few µm in projected size) embedded in a Na–Al–Si–O matrix of particles. At this degree of phase intermixing and with such small crystallite sizes, the X-ray generation volume at 15 kV is rarely confined to a single-phase crystallite, resulting in mixed-phases compositional measurements by EDS. Compositional clusters such as that shown in Fig. 2b, arise as a direct consequence of this effect. Additional information on this sample is provided in the original publication [13].

2.2 Manual Rietveld refinement of non-NASICON synthetic materials used to benchmark the accuracy of *AutoEMXSp*

a. $Bi_2Fe_4O_9$

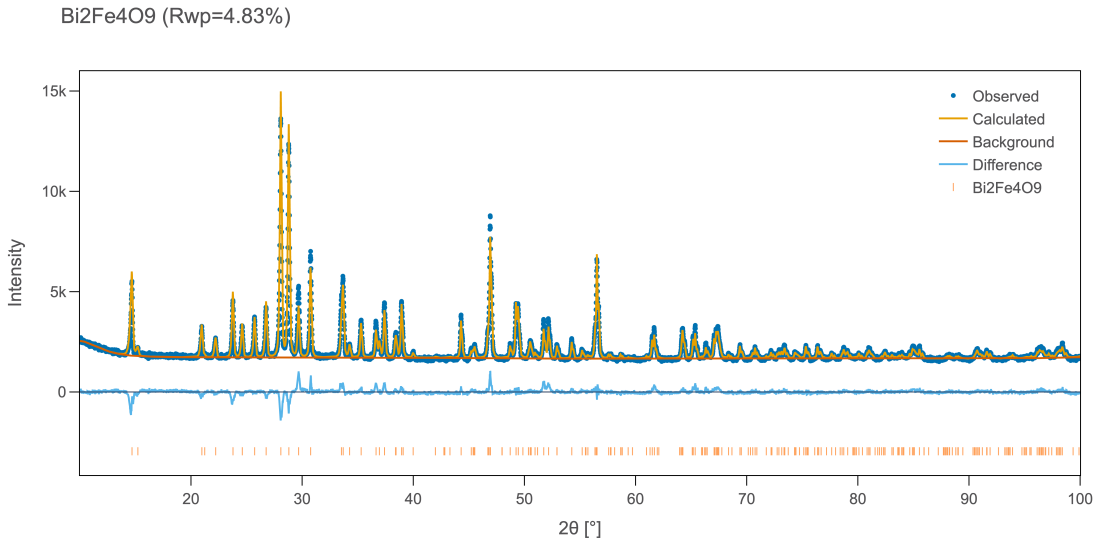

b. $Bi_{25}FeO_{39}$

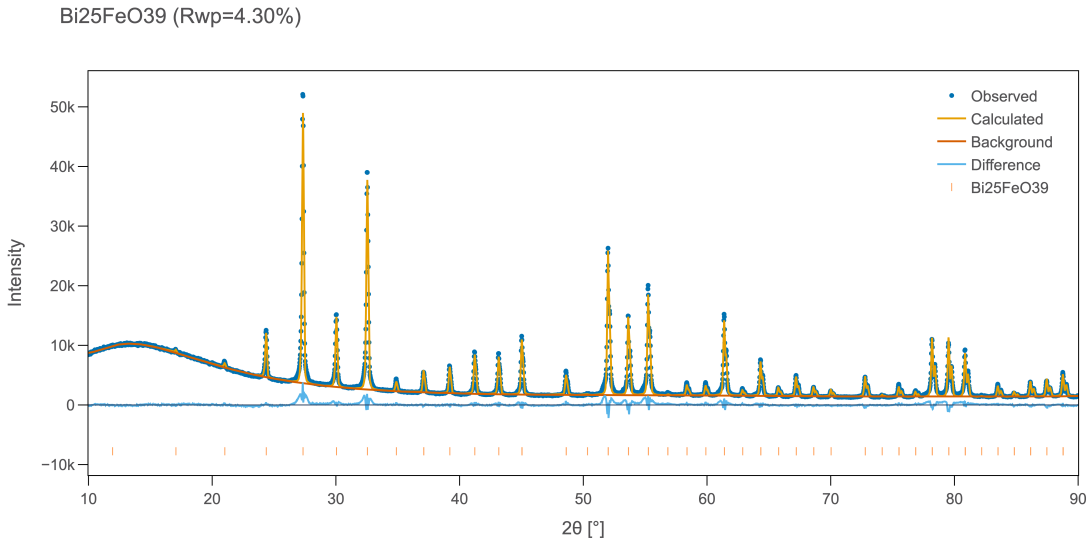

c. $CaCo(PO_3)_4$

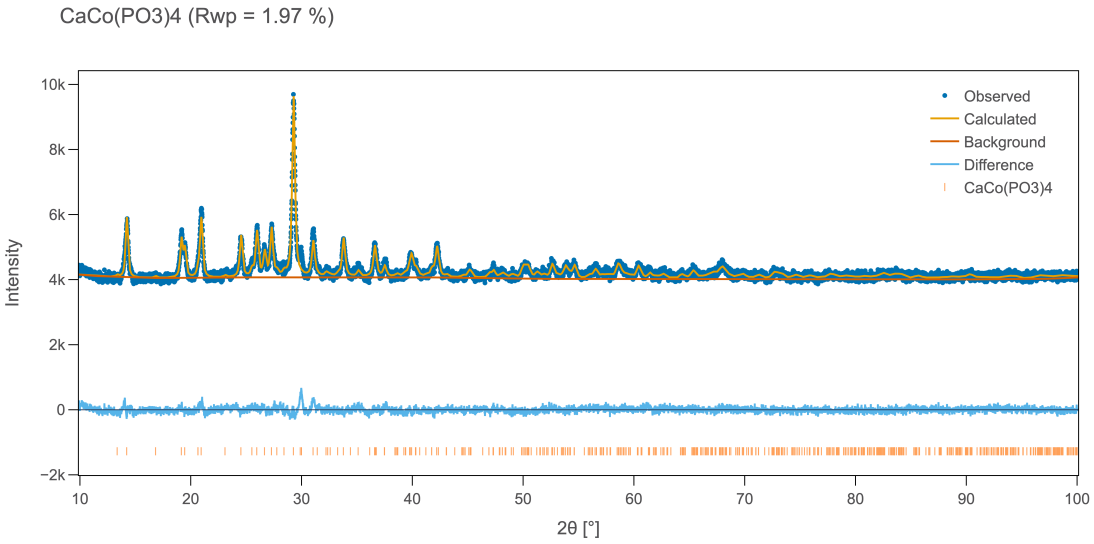

d. $Hf_2Sb_2Pb_4O_{13}$

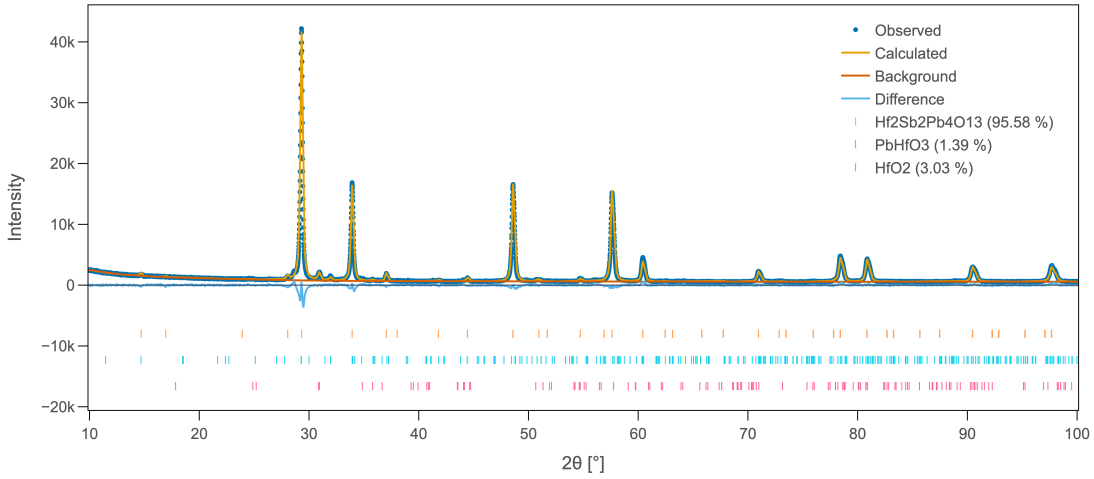

e. $K_2TiCr(PO_4)_3$

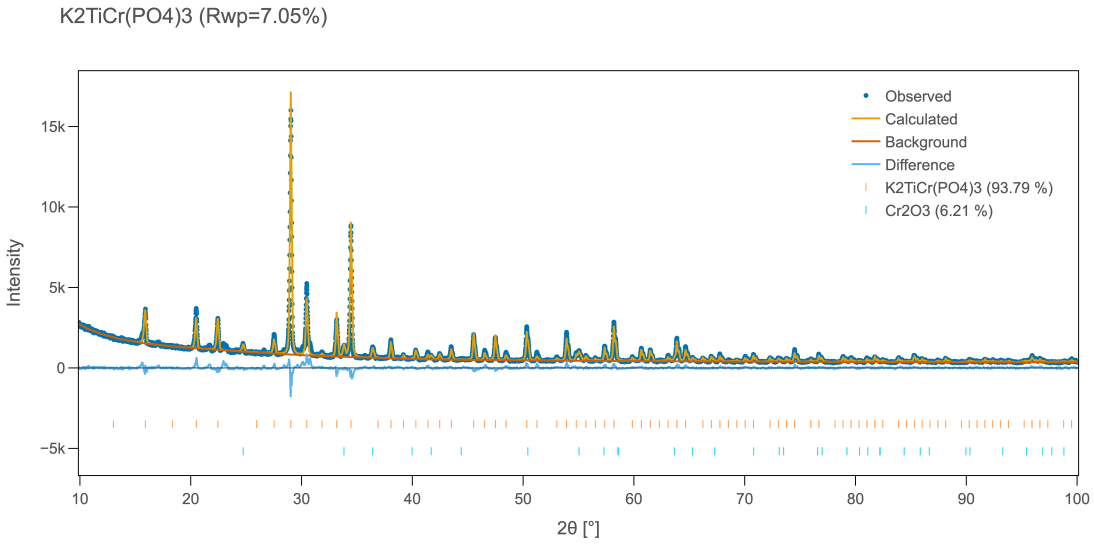

f. $K_4MgFe_3(PO_4)_5$

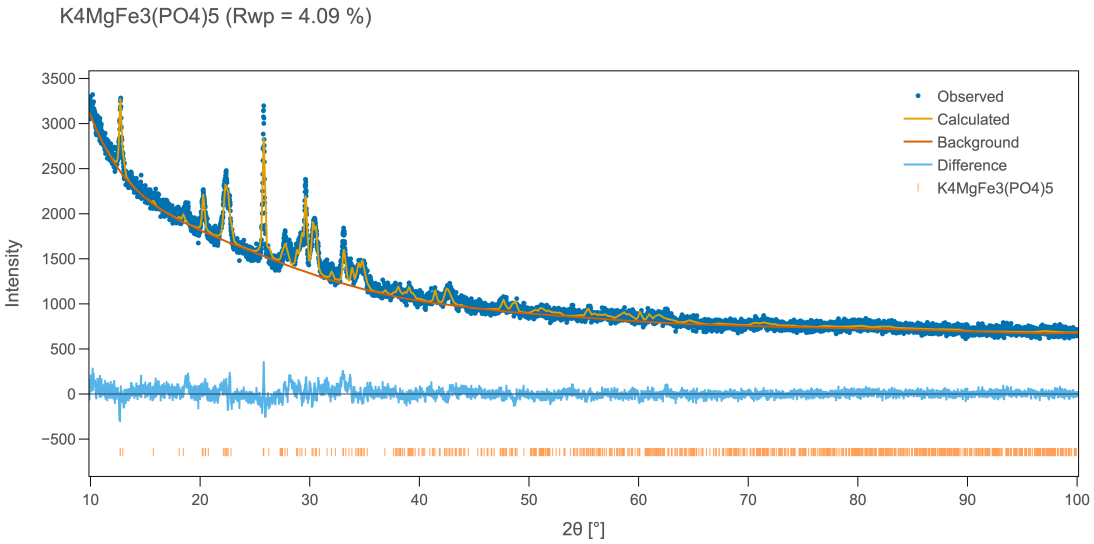

g. $KNaTi_2(PO_5)_2$

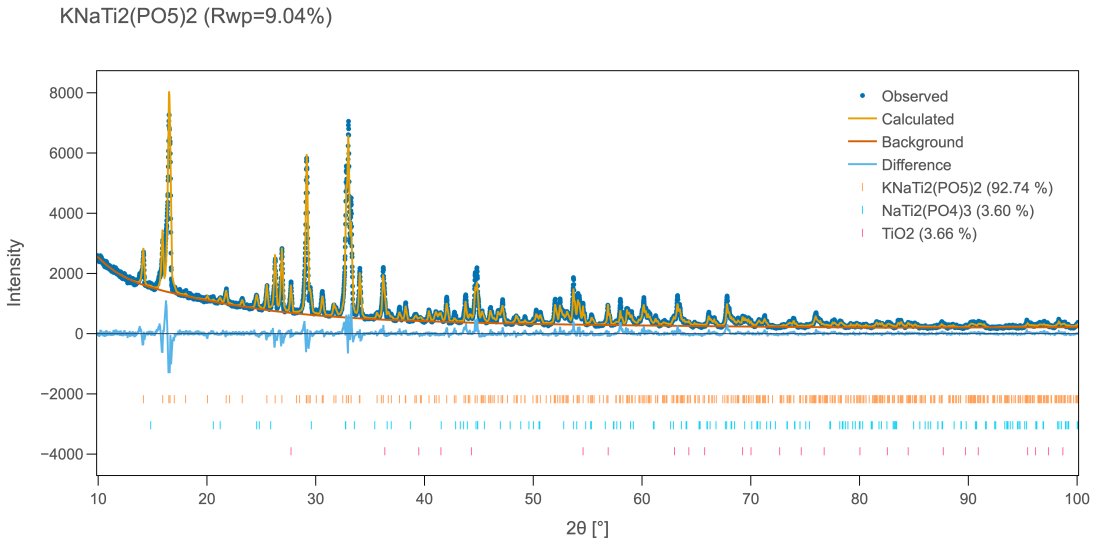

h. $LaNbO_4$

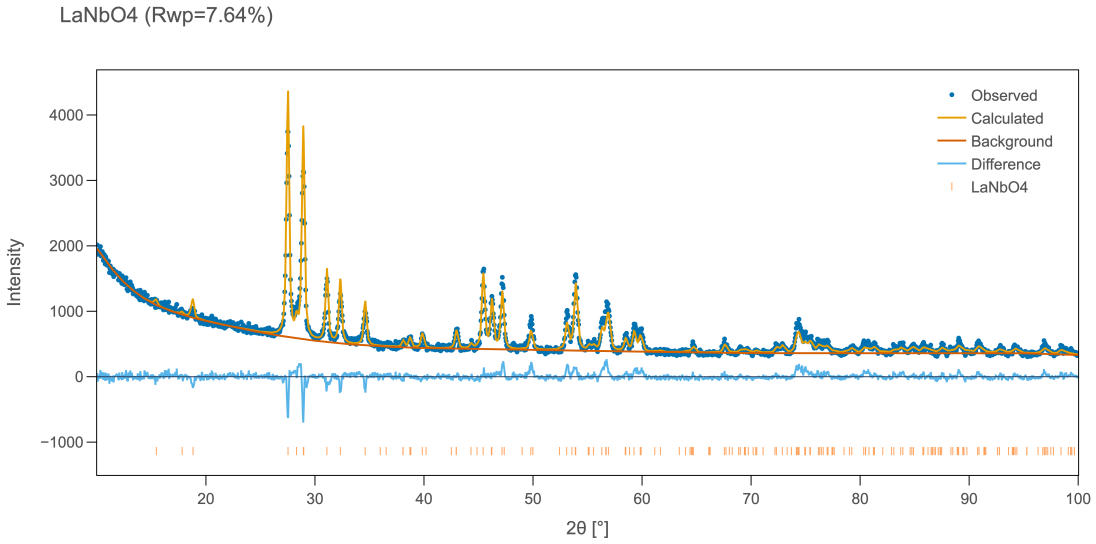

i. $MgCuP_2O_7$

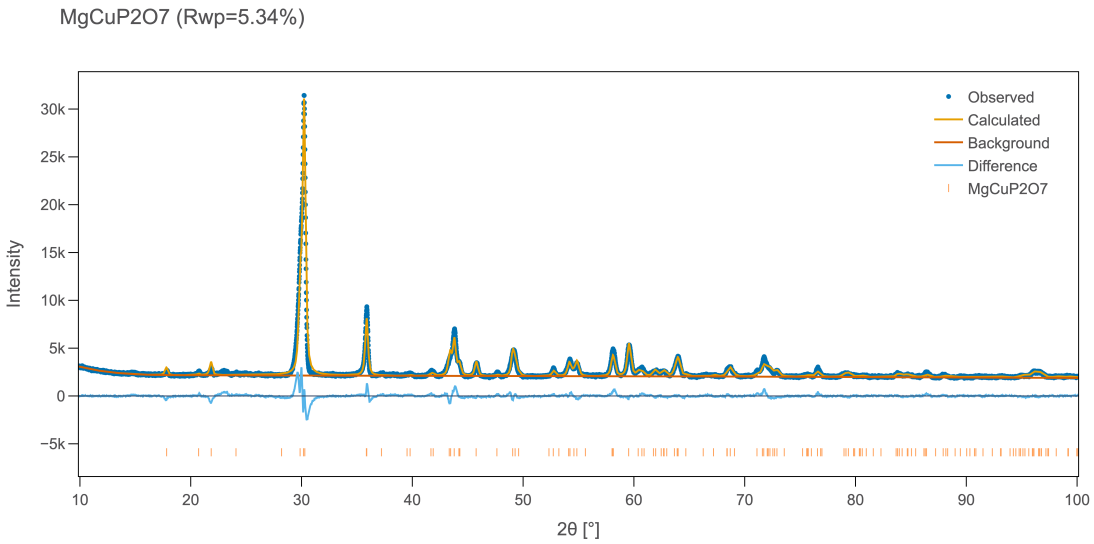

j. $MgTi_2NiO_6$

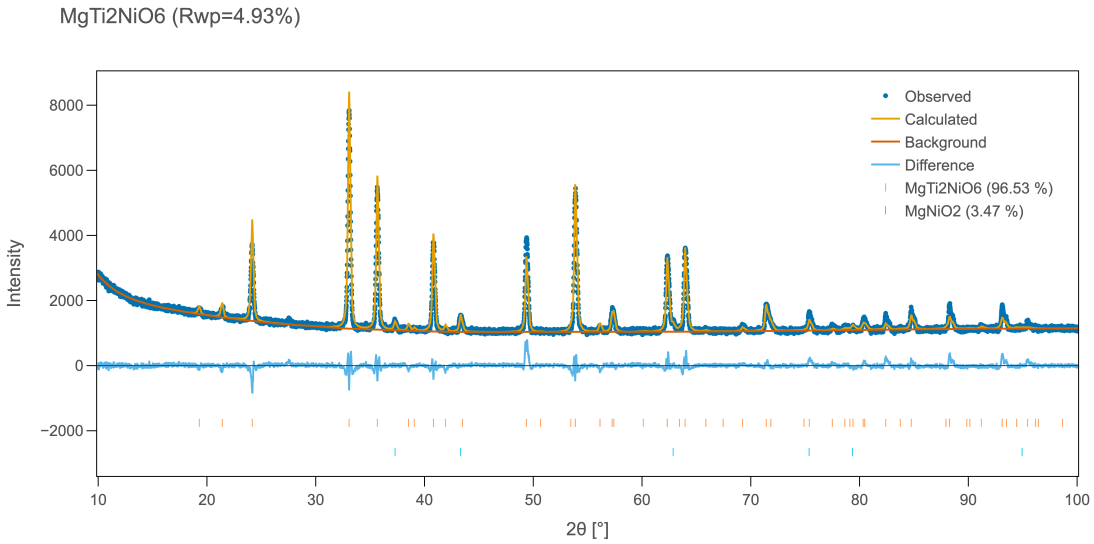

k. $MgTi_4(PO_4)_6$

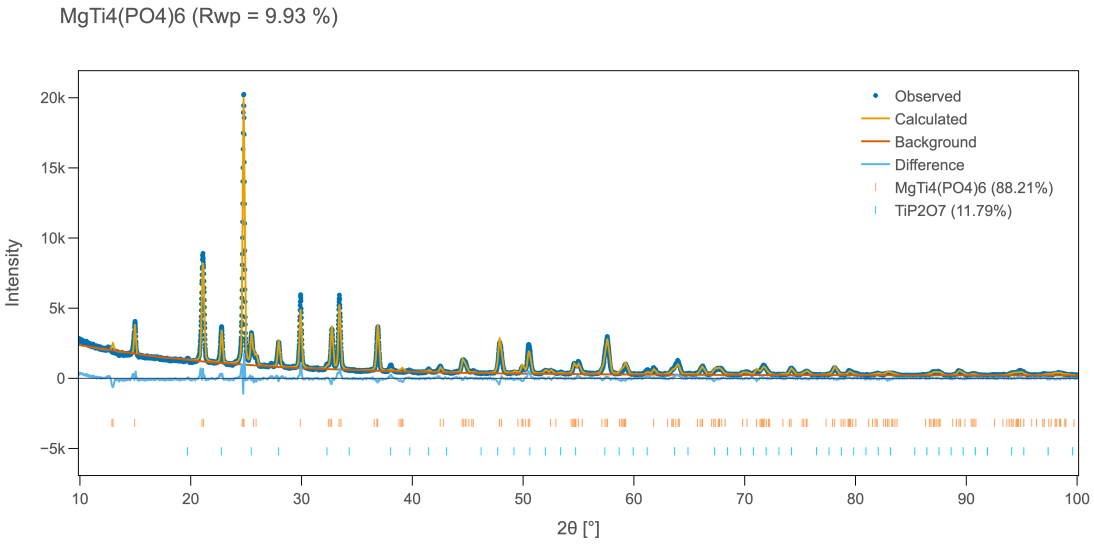

l. $MnAgO_2$

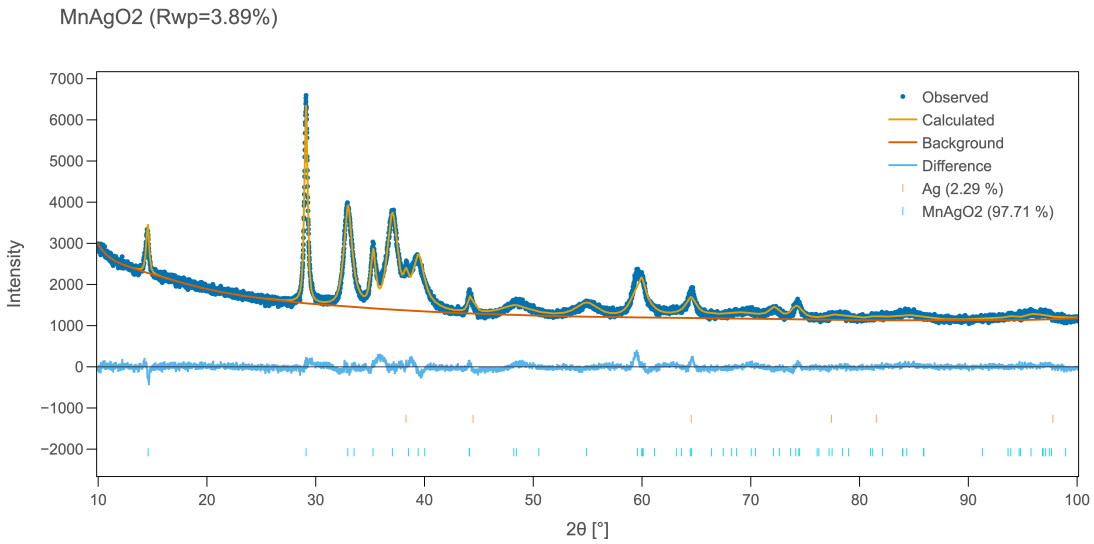

m. $NaCaMgFe(SiO_3)_4$

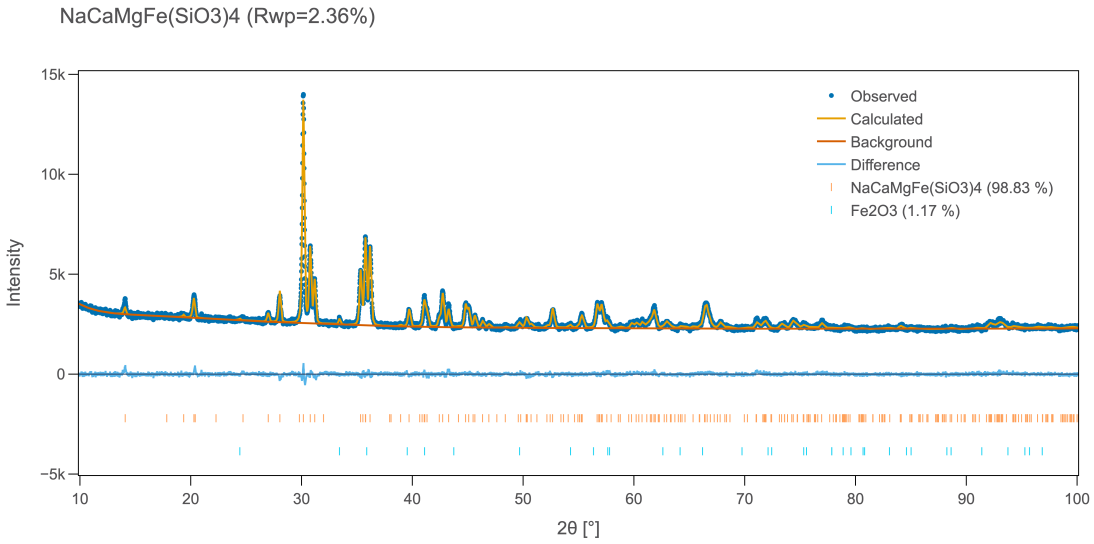

Supplementary Figure 7: **Manual Rietveld refinement of non-NASICON synthetic materials used to benchmark the accuracy of *AutoEMXSp*.** Panels **a**–**m**: Materials synthesized using the A-lab [14], indicated by a dagger (†) superscript in Tab. 1. Details of the Rietveld refinements for $Bi_2Fe_4O_9$, $Bi_{25}Fe_4O_{39}$, and $LaNbO_4$—shown in panels **a**, **b**, and **h**—are provided in Supplementary Tab. 2. The remaining materials were synthesized by Szymanski *et al.* [14]; details of their analysis are reported in the referenced work.

2.3 Manual Rietveld refinement of lab-synthesized NASICON materials used to benchmark the accuracy of *AutoEMXSp*

a. $NaGe_2(PO_4)_3$

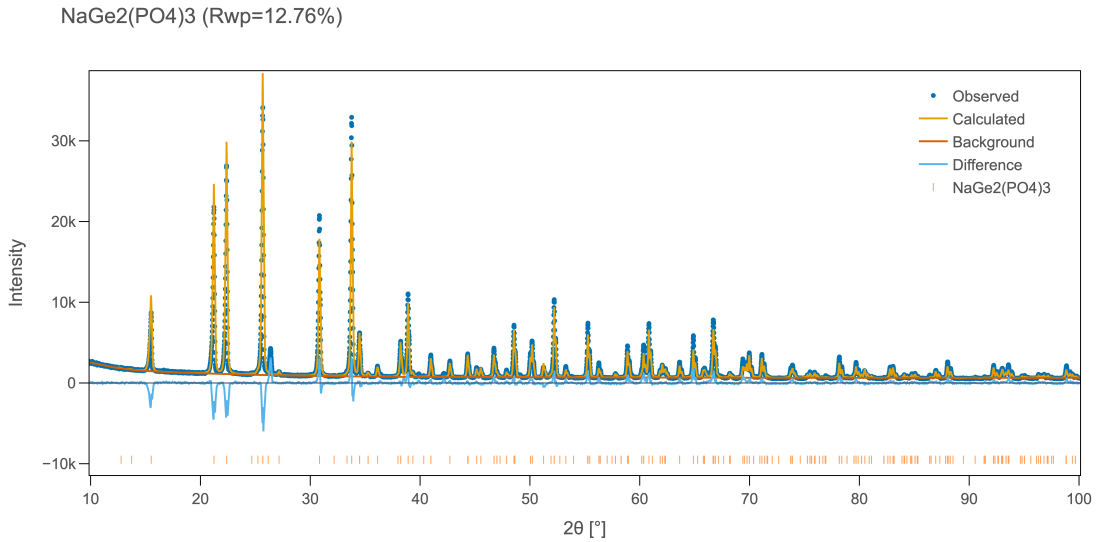

b. $NaSn_2(PO_4)_3$

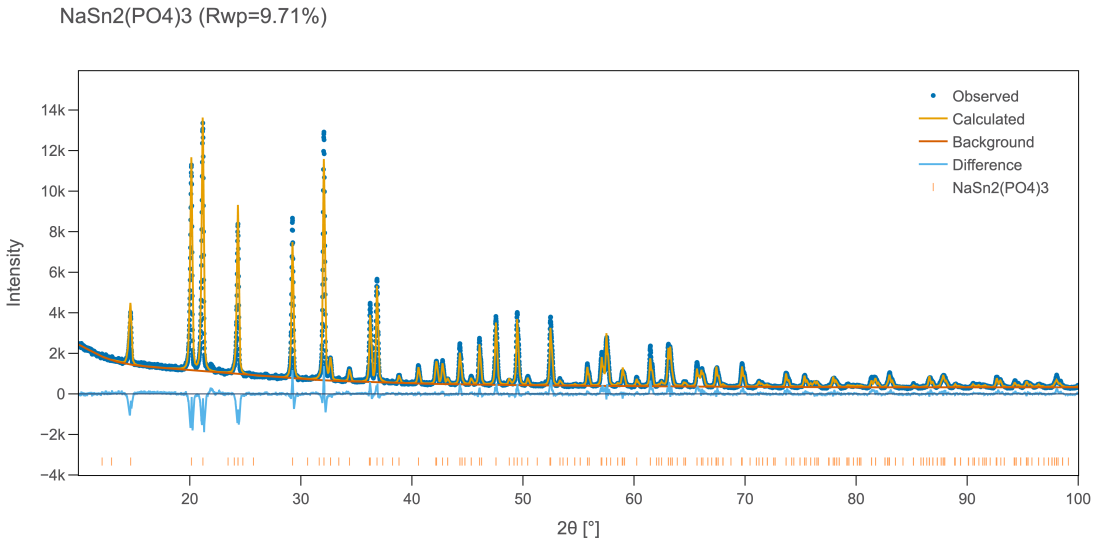

c. $NaTiSn(PO_4)_3$

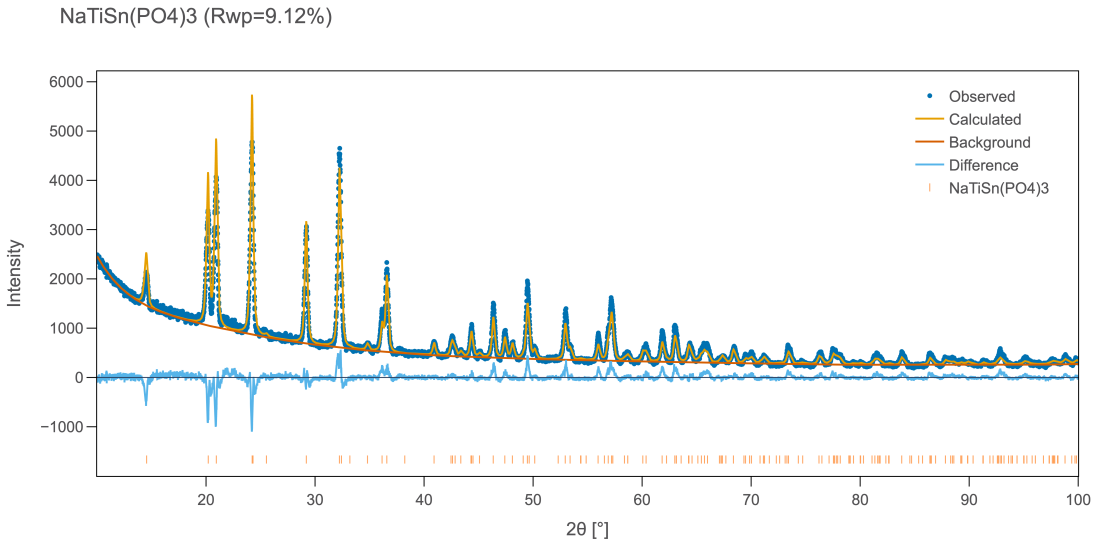

d. $NaZrTi(PO_4)_3$

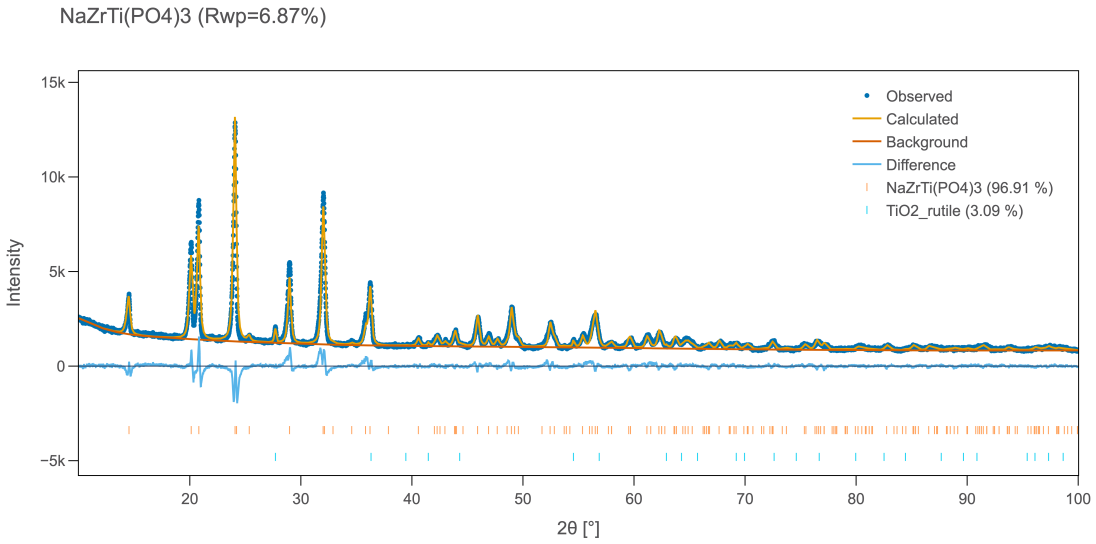

e. $Na_{0.4}Zr_{1.4}Ta_{0.6}(PO_4)_3$

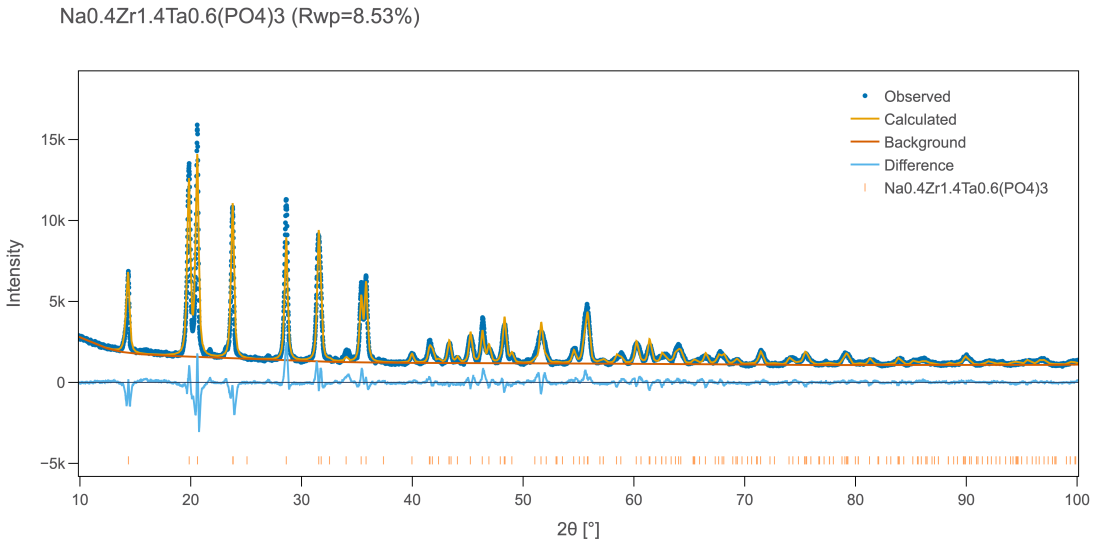

Supplementary Figure 8: **Manual Rietveld refinement of NASICON synthetic materials used to benchmark the accuracy of *AutoEMXSp*.** Panels **a**–**e**: Materials synthesized using the A-lab, indicated by a double-dagger (‡) superscript in Tab. 1. Phase verification by X-ray diffraction (XRD) was performed either by comparison against a known reference or, for more complex compositions, by analyzing the lattice parameter assuming validity of Vegard's law between the two end members [15, 16, 17, 18]. Details on the XRD refinement for each material are listed in Supplementary Tab. 2.

Supplementary Table 2: XRD Rietveld refinement lattice parameters analysis

Composition	**Analysis**
$Bi_2Fe_4O_9$	The refined lattice of the phase with Pbam space group (a = 7.979 Å, b = 8.445 Å, and c = 6.006 Å) agrees with reference ICSD 186440 (a = 7.971 Å, b = 8.439 Å, and c = 6.000 Å).
$Bi_{25}FeO_{39}$	The refined lattice of the phase with I23 space group (a = 10.190 Å) agree with reference ICSD 257493 (a = 10.191 Å).
$LaNbO_4$	The refined lattice of the phase with C2/c space group (a = 7.346 Å, b = 11.528 Å, and c = 5.206 Å) agree with reference ICSD 73390 (a = 7.340 Å, b = 11.519 Å, and c = 5.201 Å).
$NaGe_2(PO_4)_3$	The refined lattice parameters of the phase with R-3c space group (a = 8.0982 Å and c = 21.5388 Å) agree with reference (ICSD 164019, a = 8.1092 Å and c = 21.5388 Å). Despite manual phase search, a set of unidentified peaks are observed near 26.39°, 39.88°, 42.20°, and 49.06°. No impurity was found measuring this sample with *AutoEMXSp*, as shown in Supplementary Fig. 10c.
$NaSn_2(PO_4)_3$	The refined lattice parameters of the phase with R-3c space group (a = 8.5089 Å and c = 22.5159 Å) agree with reference (ICSD 72215, a = 8.5132 Å and c = 22.5106 Å).
$NaTiSn(PO_4)_3$	The refined lattice parameters of the phase with R-3c space group (a = 8.5316 Å and c = 22.0723 Å) agree with reference (ICSD 72201, a = 8.53022 Å and c = 22.10531 Å).
$NaZrTi(PO_4)_3$	$NaZrTi(PO_4)_3$: The refined lattice parameters of the phase with R-3c space group (a = 8.6461 Å and c = 22.2965 Å) agree with the linear interpolation result (a = 8.6420 Å and c = 22.2657 Å) between the two end-members: $NaZr_2(PO_4)_3$ (ICSD 193217, a = 8.7991 Å and c = 22.74096 Å) and $NaTi_2(PO_4)_3$ (ICSD 114324, a = 8.484822 Å and c = 21.7904 Å). Rutile TiO_2: The phase with rutile lattice (P42/mnm space group) has lattice parameters (a = 4.5946 Å and c = 2.9625 Å) that are slightly larger compared to the TiO_2 reference (ICSD 62677, a = 4.5926 Å and c = 2.9578 Å), indicating possible partial substitution of the six-coordinated Ti^{4+} (60.5 pm ionic radius) site by Zr^{4+} (72 pm ionic radius) ions.
$Na_{0.4}Zr_{1.4}Ta_{0.6}(PO_4)_3$	The refined lattice of the phase with R-3c space group (a = 8.75345 Å and c = 22.7019 Å) exhibits slightly reduced lattice parameters compared to the reference structure of $NaZr_2(PO_4)_3$ (ICSD 193217, a = 8.7991 Å and c = 22.74096 Å). This agrees with the expected decrease of lattice parameters due to the decrease in Na content and substitution of the larger VI coordinated Zr^{4+} ion (72 pm ionic radius) with the smaller Ta^{5+} ion (64 pm ionic radius). The absence of a significant impurity further supports the compositional accuracy. However, a set of small unidentified peaks is observed at 21.74°, 27.07°, and 33.04°. The *AutoEMXSp* result (Supplementary Fig. 10d) suggests that a Zr-rich phase might be present.

.

Composition	Analysis
Synthetic mixture from Fig. 4e, with target phase: $Na_{3.238}\,La_{0.238}\,Zr_{1.117}\,Ti_{0.645}\,(SiO_4)_2\,(PO_4)$	NASICON phase: The refined lattice parameters of the phase with C2/c space group (a = 15.7040 Å, b = 9.0905 Å, c = 9.2053 Å, β = 124.2153°, and V = 1086.6859 $Å^3$) are close to the $Na_3Zr_2(SiO_4)_2(PO_4)$ reference (ICSD 38096, a = 15.6450 Å, b = 9.0469 Å, c = 9.1796 Å, β = 123.681°, and V = 1081.1712 $Å^3$). The substitution of the VI-coordinated Zr^{4+} (72 pm ionic radius) site by La^{3+} (103.2 pm ionic radius), followed by insertion of Na^+ to charge compensate, will increase the lattice volume. The substitution of the six-coordinated Zr^{4+} (72 pm ionic radius) site by the Ti^{4+} (60.5 pm ionic radius) ions will result in a decrease of lattice volume. On the other hand, the substitution of $(PO_4)^{3-}$ polyanion group with $(SiO_4)^{4-}$ polyanion group, followed by the insertion of Na^+ to charge compensate, will increase the lattice volume. Since multiple combinations of these substitutions can contribute to lattice expansion, the observed net increase in unit cell volume relative to the ICSD reference cannot be uniquely ascribed to any specific set of substitutions using solely XRD. $Na_3La(PO_4)_2$: The refined lattice parameters ($Pca2_1$ space group, a = 14.1088 Å, b = 5.3585 Å, and c = 18.7171 Å) are close to the reference (ICSD 430499, a = 14.0830 Å, b = 5.3517 Å, and c = 18.7291 Å). Rutile TiO_2: The phase with rutile lattice (P42/mnm space group) has lattice parameters (a = 4.6034 Å and c = 2.9684 Å) that are slightly larger from the reference TiO_2 (ICSD 62677, a = 4.5926 Å and c = 2.9578 Å, indicating possible substitution of the VI-coordinated Ti^{4+} (60.5 pm) site by Zr^{4+} (72 pm) ions. ZrO_2: The phase with ZrO_2 lattice (P21/c space group) has lattice parameters (a = 5.1223 Å, b = 5.1789 Å, and c = 5.3305 Å) that are slightly smaller than the reference ZrO_2 (ICSD 41572, a = 5.1501 Å, b = 5.2077 Å, and 5.3171 Å, indicating possible substitution of the six-coordinated Zr^{4+} (72 pm radius) site by Ti^{4+} (60.5 pm radius) ions.

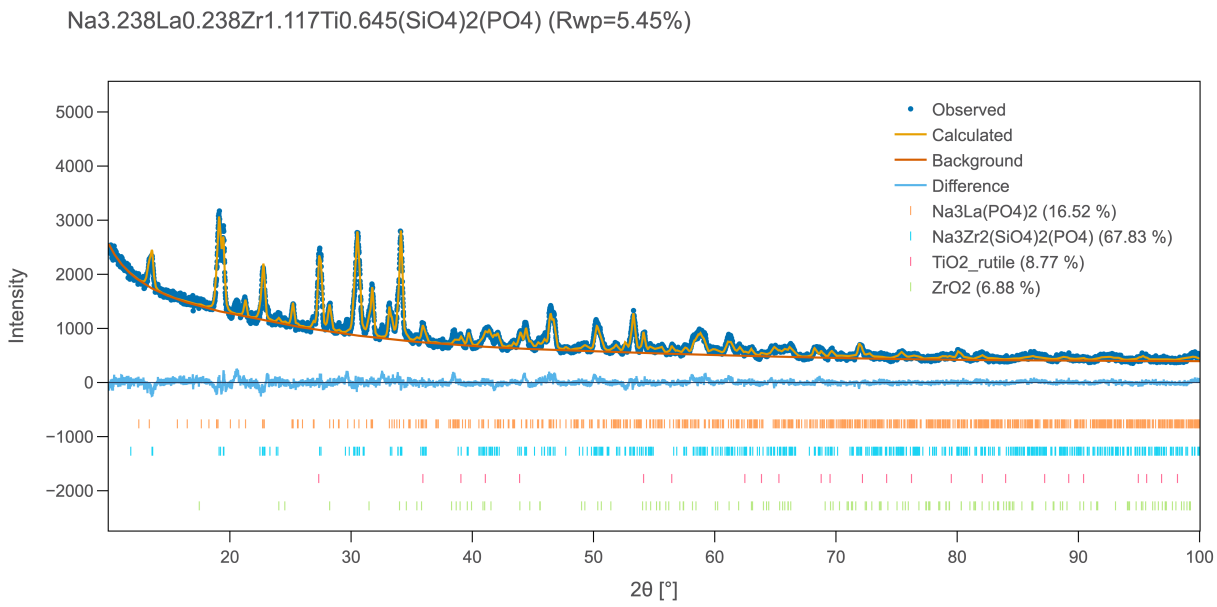

Supplementary Figure 9: **Manual XRD Rietveld refinement of the multi-phase synthetic product analyzed in Fig. 4e.** The sample was formed by heating a mix of Na_2CO_3, La_2O_3, ZrO_2, TiO_2, SiO_2, and $NH_4H_2PO_4$ with ratio corresponding to the overall composition of $Na_{3.238}\,La_{0.238}\,Zr_{1.117}\,Ti_{0.645}\,(SiO_4)_2\,(PO_4)$, using 10% Na excess to compensate for Na loss during the reaction. The XRD refinement indicates the presence of a NASICON phase with nominal composition $Na_3Zr_2(SiO_4)_2(PO_4)_3$; excluding this phase results in a considerably worse fit (R_{wp} = 14.89% instead of 5.49%) with no plausible alternative phases to account for the observed peaks. However, the measured NASICON phase is likely off-stoichiometric, indicated by a slight enlargement of lattice parameters (Supplementary Tab. 2). Its accurate composition cannot be determined from lattice parameters alone, given the presence of significant impurities and the multiple possible compositions compatible with the observed cell dimensions. Here, *AutoEMXSp* provides additional insight, confirming the incorporation of less than 1 *at*% Ti and La into the NASICON phase–as reported in Fig. 4e–and off-stoichiometry Si (11.1±0.7 *at*% instead of 10 *at*%) and P (3.5±1.2 *at*% instead of 5 *at*%). These measurements agree with an enlargement of lattice parameter, as detailed in Supplementary Tab. 2.

3 *AutoEMXSp* outputs

Supplementary Table 3: **Full output compositions of samples described in the main manuscript. a**, Intermixed $NaAlSiO_4$ + $LiMn_{1.5}Ni_{0.5}O_4$ from Fig. 2b. **b**, K-412 NIST standard from Fig. 4a. **c**, NASICON $NaZrTi(PO_4)_3$ from Fig. 4d. **d**, NASICON synthethic mixture from Fig. 4e.

a. Intermixed $NaAlSiO_4$ + $LiMn_{1.5}Ni_{0.5}O_4$ from Fig. 2b

	# pts	Si (*at*%)	Ni (*at*%)	Al (*at*%)	Mn (*at*%)	Na (*at*%)	O (*at*%)
●	42	10.4 ± 2.5	3.7 ± 1.7	8.8 ± 1.9	10.5 ± 4.7	7.7 ± 1.9	58.9 ± 2.1

	Ref.	CS_{mix}
●	$NaAlSiO_4$ + $LiMn_{1.5}Ni_{0.5}O_4$	0.83

b. K-412 NIST standard from Fig. 4a

	# pts	Fe (*at*%)	Mg (*at*%)	Ca (*at*%)	Al (*at*%)	Si (*at*%)	O (*at*%)
●	51	3.1 ± 0.3	10.1 ± 0.5	5.9 ± 0.3	4.2 ± 0.2	16.6 ± 0.7	60.1 ± 1.0
●	5	0.1 ± 0.1	0.6 ± 0.7	0.3 ± 0.3	0.5 ± 0.2	31.9 ± 1.2	66.6 ± 2.1

	Ref.	CS_{cnd}
●	K-412 NIST std	0.95
●	SiO_2	0.86

c. NASICON $NaZrTi(PO_4)_3$ from Fig. 4d

	# pts	Na (*at*%)	Zr (*at*%)	Ti (*at*%)	P (*at*%)	O (*at*%)
●	36	5.6 ± 0.4	5.5 ± 0.8	5.1 ± 0.9	16.1 ± 0.9	67.8 ± 0.8
●	2	1.8 ± 0.5	2.1 ± 1.2	25.5 ± 3.3	5.5 ± 1.5	65.1 ± 0.1

	Ref. / Mix	CS_{cnd}	CS_{mix}
●	$NaZrTi(PO_4)_3$	0.91	
●	$NaZrTi(PO_4)_3$ + TiO_2		0.98

d. NASICON synthethic mixture from Fig. 4e

	# pts	Na (*at*%)	La (*at*%)	Zr (*at*%)	Ti (*at*%)	Si (*at*%)	P (*at*%)
●	8	21.2 ± 2.1	7.0 ± 0.4	0.1 ± 0.1	–	0.5 ± 0.4	14.9 ± 1.2
●	7	1.0 ± 0.7	–	1.4 ± 0.5	31.3 ± 2.2	0.3 ± 0.2	0.4 ± 0.4
●	14	15.2 ± 1.4	0.4 ± 0.7	8.3 ± 0.7	0.9 ± 0.9	11.1 ± 0.7	3.5 ± 1.2
●	7	4.9 ± 2.6	0.6 ± 1.4	17.2 ± 5.7	2.6 ± 2.8	3.6 ± 3.2	0.4 ± 0.9
●	3	10.6 ± 2.9	7.4 ± 4.2	3.7 ± 3.6	16.2 ± 4.4	0.5 ± 0.3	2.9 ± 4.5

	O (*at*%)	Ref. / Mix	CS_{cnd}	CS_{mix}
●	56.4 ± 1.5	$Na_3La(PO_4)$	0.94	
●	65.6 ± 1.9	TiO_2	0.63	
●	60.7 ± 2.2	$Na_3Zr_2(SiO_4)_2(PO_4)$	0.64	
●	70.8 ± 3.1	ZrO_2 + $Na_3Zr_2(SiO_4)_2(PO_4)$		0.31
●	58.8 ± 3.5	TiO_2 + $Na_3La(PO_4)_2$		0.43

a. $Bi_2Fe_4O_9$

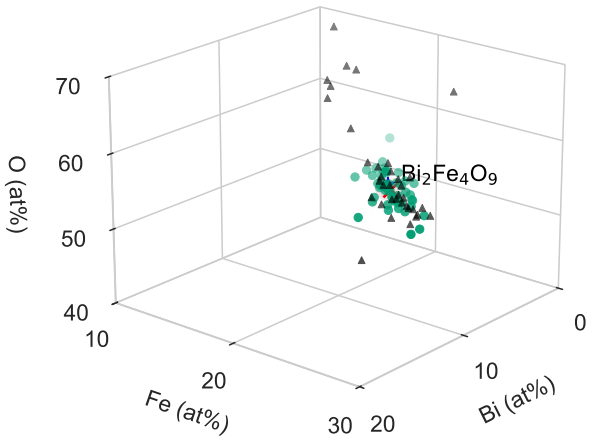

	# pts	Bi (*at*%)	Fe (*at*%)	O (*at*%)	Ref. (CS_{cnd})
●	51	13.5 ± 0.8	27.0 ± 1.1	59.6 ± 1.5	$Bi_2Fe_4O_9$ (0.98)

b. $NaCaMgFe(SiO_3)_4$

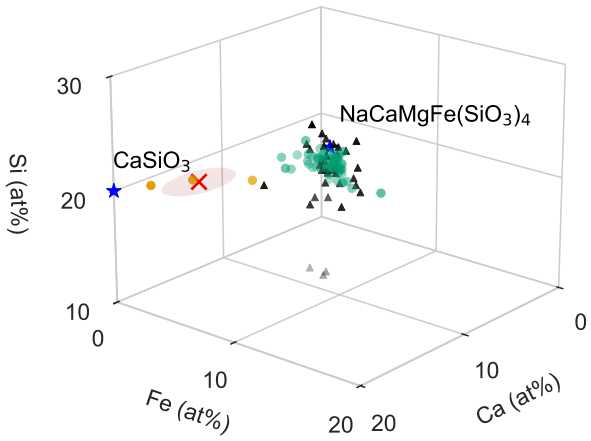

	# pts	Ca ($at\%$)	Na ($at\%$)	Mg ($at\%$)	Fe ($at\%$)	Si ($at\%$)	O ($at\%$)
●	54	5.6 ± 0.7	4.9 ± 0.7	4.9 ± 0.9	5.3 ± 1.1	18.8 ± 0.9	60.5 ± 1.3
●	3	14.1 ± 3.1	2.3 ± 0.6	1.6 ± 0.7	1.7 ± 1.6	19.1 ± 0.4	61.3 ± 0.8

	Ref. (CS)
●	$NaCaMgFe(SiO_3)_4$ (0.88)
●	$NaCaMgFe(SiO_3)_4 + CaSiO_3$ (0.98)

c. NASICON $NaGe_2(PO_4)_3$

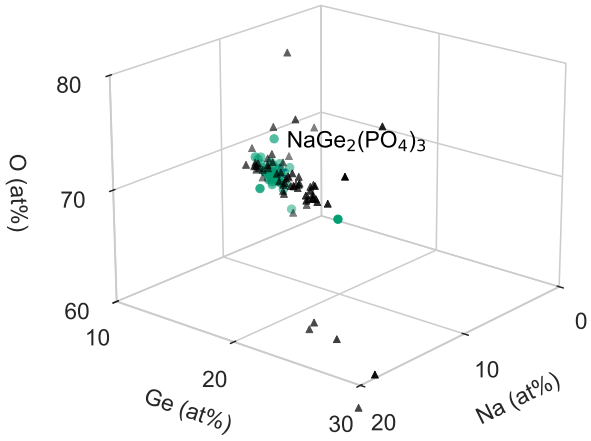

	# pts	Na ($at\%$)	Ge ($at\%$)	P ($at\%$)	O ($at\%$)	Ref. (CS_{cnd})
●	36	5.8 ± 0.5	10.9 ± 0.9	16.8 ± 0.7	66.5 ± 1.1	$NaGe_2(PO_4)_3$ (0.99)

d. NASICON $Na_{0.4}Zr_{1.4}Ta_{0.6}(PO_4)_3$

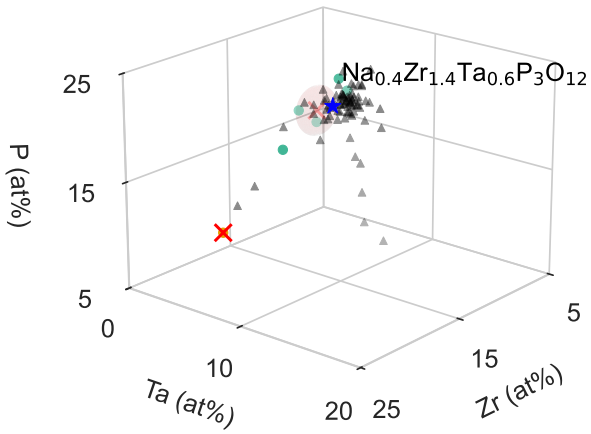

	# pts	Na ($at\%$)	Zr ($at\%$)	Ta ($at\%$)	P ($at\%$)	O ($at\%$)
●	5	2.4 ± 0.7	8.8 ± 1.8	2.7 ± 1.1	16.9 ± 2.4	69.3 ± 1.6
●	1	2.6	16.7	0.9	7.3	72.4

	Ref. (CS_{cnd})
●	$Na_{0.4}Zr_{1.4}Ta_{0.6}(PO_4)_3$ (0.92)
●	–

e. Alamosite mineral ($PbSiO_3$)

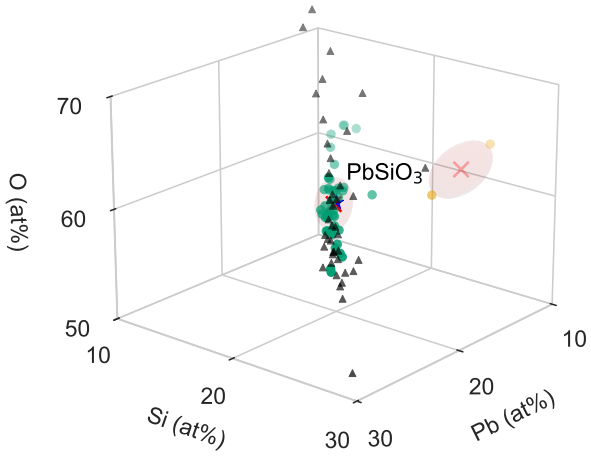

	# pts	Pb ($at\%$)	Si ($at\%$)	O ($at\%$)	Ref. (CS_{cnd})
●	46	20.2 ± 1.4	19.9 ± 1.1	59.9 ± 2.4	$PbSiO_3$ (1.00)
●	2	13.20 ± 3.2	24.80 ± 0.8	62.00 ± 2.4	–

f. Labradorite mineral ($(Ca_{0.65}Na_{0.34})(Al_{1.66}Si_{2.33})O_8$)

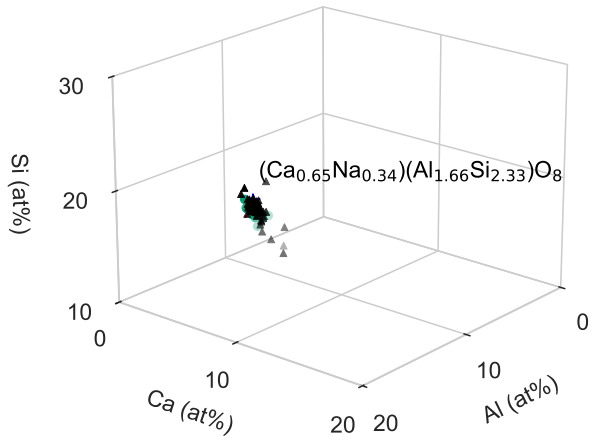

	# pts	Na ($at\%$)	Al ($at\%$)	Ca ($at\%$)	Si ($at\%$)	O ($at\%$)
●	26	2.6 ± 0.1	12.9 ± 0.6	5.0 ± 0.3	17.2 ± 0.8	62.2 ± 1.6

	Ref. (CS_{cnd})
●	$(Ca_{0.65}Na_{0.34})(Al_{1.66}Si_{2.33})O_8$ (0.95)

g. $Ba_3(PO_4)_2$ commercial powder

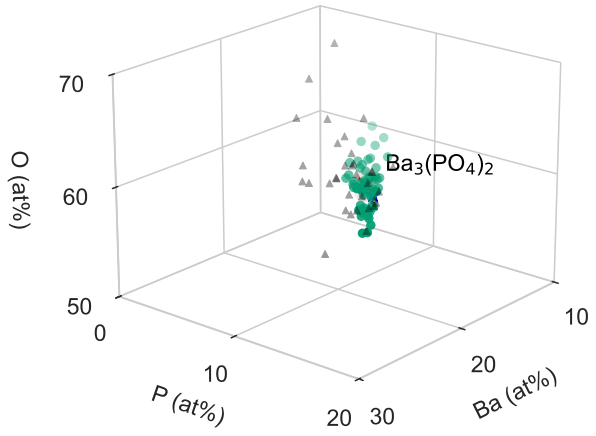

	# pts	Ba ($at\%$)	P ($at\%$)	O ($at\%$)	Ref. (CS_{cnd})
●	57	23.0 ± 0.9	14.8 ± 0.7	62.2 ± 1.5	$Ba_3(PO_4)_2$ (0.96)

h. PbO commercial powder

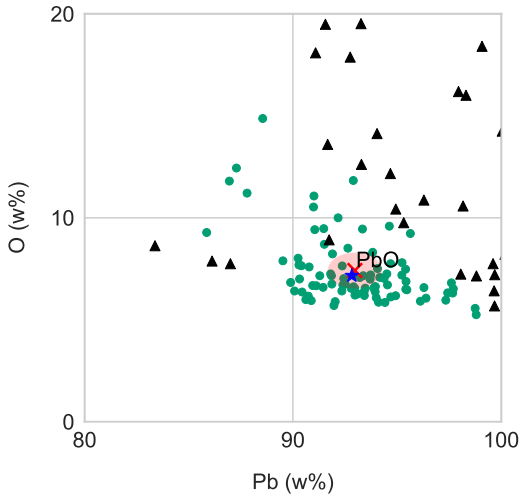

Using *AutoEMXSp* background model f_B, from Eq. (9).

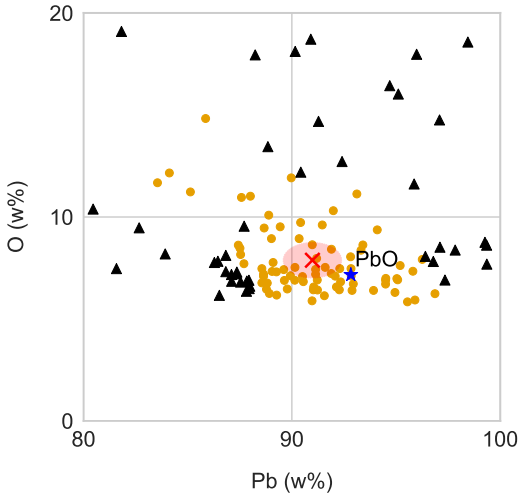

Using uncorrected Duncumb's model $f_{B,Duncumb}$ [7], reported in Eq. (7).

	# pts	Pb (*at*%)	O (*at*%)	Ref. (CS_{cnd})
●	87	49.8 ± 5.3	50.2 ± 5.3	PbO (1.00)
●	78	47.7 ± 5.3	52.3 ± 5.3	PbO (0.80)

Supplementary Figure 10: **Selection of *AutoEMXSp* characterization outputs for single-phase samples from Tab. 1 analyzed in Fig. 3. a**, A-lab synthesized $Bi_2Fe_4O_9$. **b**, A-lab synthesized $NaCaMgFe(SiO_3)_4$, containing trace $CaSiO_3$ impurity. **c**, A-lab synthesized NASICON $NaGe_2(PO_4)_3$. **d**, A-lab synthesized NASICON $Na_{0.4}Zr_{1.4}Ta_{0.6}(PO_4)_3$. **e**, Alamosite ($PbSiO_3$) mineral. **f**, Labradorite ($(Ca_{0.65}Na_{0.34})(Al_{1.66}Si_{2.33})O_8$) mineral. **g**, $Ba_3(PO_4)_2$ commercial powder **h**, PbO commercial powder, also showing the results obtained if Duncumb's background model (Eq. (7)) were applied without the correction introduced in this work–i.e., Eq. (9).

Supplementary Information References

[1] Peter J. Statham. Pitfalls in linear and non-linear profile-fitting procedures for resolving severely overlapped peaks. *X-Ray Spectrometry*, 7(3):132–137, 1978.

[2] R H Redus and A C Huber. Response Function of Silicon Drift Detectors for Low Energy X-rays. In *Advances in X-ray Analysis (AXA)*, pages 274–282. International Centre for Diffraction Data (ICDD), 2015.

[3] J. Osán, J. de Hoog, P. Van Espen, I. Szalóki, C.-U. Ro, and R. Van Grieken. Evaluation of energy-dispersive x-ray spectra of low-Z elements from electron-probe microanalysis of individual particles. *X-Ray Spectrometry*, 30(6):419–426, nov 2001.

[4] P. Statham, C. Penman, and P. Duncumb. Improved spectrum simulation for validating SEM-EDS analysis. *IOP Conference Series: Materials Science and Engineering*, 109(1):0–10, 2016.

[5] Andrzej A. Markowicz and Rene E. Van Grieken. Composition dependence of bremsstrahlung background in electron-probe x-ray microanalysis. *Analytical Chemistry*, 56(12):2049–2051, oct 1984.

[6] János L. Lábár and Szabina Török. A peak-to-background method for electron-probe x-ray microanalysis applied to individual small particles. *X-Ray Spectrometry*, 21(4):183–190, jul 1992.

[7] Peter Duncumb, Ian R. Barkshire, and Peter J. Statham. Improved X-ray Spectrum Simulation for Electron Microprobe Analysis. *Microscopy and Microanalysis*, 7(4):341–355, jul 2001.

[8] Nikolay Semenovich Karmanov, Sergei Vasilievich Kanakin, and Yuri Grigorievich Lavrent'ev. Integral bremsstrahlung energy as an inbuilt standard in energy-dispersive electron probe microanalysis. *X-Ray Spectrometry*, 51(5-6):444–453, 2022.

[9] Joseph I. Goldstein, Dale E. Newbury, Joseph R. Michael, Nicholas W.M. Ritchie, John Henry J. Scott, and David C. Joy. *Scanning Electron Microscopy and X-Ray Microanalysis*. Springer New York, New York, NY, 2018.

[10] Mouad Essani, Emmanuelle Brackx, and Emmanuel Excoffier. A method for the correction of size effects in microparticles using a peak-to-background approach in electron-probe microanalysis. *Spectrochimica Acta - Part B Atomic Spectroscopy*, 169(May):105880, 2020.

[11] Gustavo Castellano, János Osán, and Jorge Trincavelli. Analytical model for the bremsstrahlung spectrum in the 0.25–20 keV photon energy range. *Spectrochimica Acta Part B: Atomic Spectroscopy*, 59(3):313–319, mar 2004.

[12] John A. Small, Stefan D. Leigh, Dale E. Newbury, and Robert L. Myklebust. Modeling of the bremsstrahlung radiation produced in pure-element targets by 10–40 keV electrons. *Journal of Applied Physics*, 61(2):459–469, jan 1987.

[13] Shilong Wang, Nathan J. Szymanski, Yuxing Fei, Yan Zeng, Michael Whittaker, and Gerbrand Ceder. Direct Li-ion Cathode Synthesis from α-Spodumene through Solid-State Reaction. *Submitted*, 2025.

[14] Nathan J. Szymanski, Bernardus Rendy, Yuxing Fei, Rishi E. Kumar, Tanjin He, David Milsted, Matthew J. McDermott, Max Gallant, Ekin Dogus Cubuk, Amil Merchant, Haegyeom Kim, Anubhav Jain, Christopher J. Bartel, Kristin Persson, Yan Zeng, and Gerbrand Ceder. An autonomous laboratory for the accelerated synthesis of novel materials. *Nature*, 624(7990):86–91, 2023.

[15] C. P. Kempter. Vegard's "law". *physica status solidi (b)*, 18(2):K117–K118, jan 1966.

[16] Hashlina Rusdi, Roshidah Rusdi, Shujahadeen B Aziz, Abdullah Saad Alsubaie, Khaled H Mahmoud, and Mohd F Z Kadir. The Role of Sintering Temperature and Dual Metal Substitutions (Al3+, Ti4+) in the Development of NASICON-Structured Electrolyte. *Materials*, 14(23):7342, nov 2021.

[17] Hongzhi Zhang, Yuchang Su, Jing Zhang, Zihui Ni, and Xinmin Zhang. Controllable structural ordering via chemical substitution to the efficient and thermally stable luminescence in NASICON-type phosphor Series: $Na_{1+x}Hf_{2-x}Sc(PO_4)_3$:Eu. *Chemical Engineering Journal*, 426(May):130778, dec 2021.

[18] Elena Asabina, Vladislav Sedov, Vladimir Pet'kov, Dina Deyneko, and Andrey Kovalsky. Synthesis, structure and luminescence properties of the europium-containing NASICON type phosphates. *Journal of Sol-Gel Science and Technology*, 105(2):547–554, feb 2023.